# Combining seismic signal dynamic inversion and numerical modeling improves landslide process reconstruction

Yan Yan[a,c], Yifei Cui[b]*, Jiaojiao Zhou[a], Xinghui Huang[d], Wengang Zhang[e], Shuyao Yin[a], Jian Guo[b], ~~Jiaojiao Zhou[a],~~ Sheng Hu[f]

[a] Key Laboratory of High-Speed Railway Engineering, MOE/School of Civil Engineering, Southwest Jiaotong University, Chengdu 610031, China

[b] State Key Laboratory of Hydroscience and Engineering, Tsinghua University, Beijing 100084, China

[c] Institute of Geographic Sciences and Natural Resources Research, Chinese Academy of Sciences, Beijing 100101, China

[d] China Earthquake Networks Center, Beijing 100045, China

[e] School of Civil Engineering, Chongqing University, Chongqing 400045, China

[f] College of Urban and Environmental Sciences, Northwest University, Xi'an 710127, China

*Corresponding author: Yifei Cui, e-mail: yifeicui@mail.tsinghua.edu.cn

样式定义: 题注

## Abstract

Landslides present a significant hazard for humans, but continuous landslide monitoring is not yet possible due to their unpredictability. In recent years, numerical simulation and seismic inversion method have been used to provide valuable data for understanding the entire process of landslide movement. However, each method has shortcomings. Dynamic inversion based on long-period seismic signals gives the force-time history of landslide using empirical Green's function, but lack of detailed flowing characteristics of the hazards. Numerical simulation can simulate the entire movement process, but results are strongly influenced by choice of modelling parameters. Therefore, developing a method for combining those two techniques has become a focus for research in recent years. In this study, we develop such a protocol based on analysis of the 2018 Baige landslide in China. Seismic signal inversion results are used to constrain and optimize the numerical simulation. We apply the procedure to the Baige event and, combined with field/geological survey, show it provides a comprehensive and accurate method for dynamic process reconstruction. We found that the Baige landslide was triggered by detachment of the weathered layer, with severe top fault segmentation. The landslide process comprised four stages: initiation, main slip, blocking, and deposition. Multi-method mutual verification effectively reduces the inherent drawbacks of each method, and multi-method joint analysis improves the rationality and reliability of the results. The approach outlined in this study could help better understand the landslide dynamic

process.

~~Landslides present a significant hazard for humans, but continuous landslide monitoring is not yet possible due to their unpredictability. Post-event reconstruction based on field survey and remote sensing cannot provide full insight into the landslide movement process. Analysis and inversion of the seismic signals generated by landside movement has started to provide valuable data for understanding the entire process of landslide movement, from initiation to cessation, along with numerical simulation, but each method has shortcomings. Simple seismic signal analysis can detect landslide occurrence, but the propagation effect generates lags. Dynamic inversion based on long-period seismic signals gives the low-frequency curve of landslide dynamic parameters, but not the high-frequency characteristics. Numerical simulation can simulate the entire movement process, but results are strongly influenced by choice of model parameters. Developing a method for combining the three techniques has become a focus for research in recent years. Here, we develop such a protocol based on analysis of the 2018 Baige landslide (China). Seismic signal dynamic inversion results are used to verify the numerical simulation, and then the numerical simulation is dynamically constrained and optimized to obtain the best numerical simulationsvalue. We apply the procedure to the Baige event and, combined with field/geological survey, show it provides a comprehensive and accurate method for dynamic process reconstruction. We found that the Baige landslide was triggered by detachment of the weathered layer, with severe top fault~~

segmentation. The landslide process comprised four stages: initiation, main slip, blocking, and deposition. Multi-method mutual verification effectively reduces the inherent ambiguity of each method, and multi-method joint analysis improves the rationality and reliability of the results. The approach outlined in this study could help better understand the landslide dynamic process.The approach outlined in this study could be used to support hazard prevention and control in sensitive areas.

**Keywords:** Landslide processes reconstruction, Seismic signal analysis, Dynamic inversion, Numerical simulation, 2018 “10.10” Baige Landslide.

## 1. Introduction

Landslides present a significant hazard for humans, the number of fatalities resulting from non-seismic landslides between 2004 and 2016 averaged 4,000 per yearbeing responsible for an average of 4,000 deaths per year between 2004 and 2016 (Froude and Petley, 2018). However, they cannot be continuously monitored due to their unpredictability and difficulty of detection (Chen et al., 2013; Yamada et al., 2013; Feng et al., 2016; Wang et al., 2020b), and the landslide movement process cannot be fully understood through post-event field investigation and remote sensing alone. Hence, to aid warning and prevention of landslide hazards and reduce associated losses, there is an urgent need to develop alternative methods to enable in-depth investigation of the dynamic characteristics of landslide generation and movement.

Landslide movement generates seismic signals that propagate to the surrounding area. The development of environmental seismology and construction of global seismic networks

(Dammeier et al., 2016) means the seismic signals generated by landslide movement can be quantitatively recorded by nearby seismic stations (Walter et al., 2012; Yamada et al., 2012; Chen et al., 2013; Yamada et al., 2013). Seismic signals generated by landslides reflect the duration, location, and scale of the event (Kao et al., 2012; Yamada et al., 2012; Chen et al., 2013); seismic signal analysis is increasingly used for landslide hazard monitoring and early warning, but it also offers a research tool for understanding landslide dynamics. The size and location of landslides can be estimated from the amplitude, frequency range, and time-frequency spectrum of the seismic signal (Favreau et al., 2010; Moretti et al., 2012; Moretti et al., 2015), along with timing of the event (Sakals et al., 2011; Zhang et al., 2019), and landslide dynamics (Yamada et al., 2013; Hibert et al., 2015; Jiang et al., 2016). The method of detecting, locating, and identifying landslide events using broadband seismograph records is based on associating seismic signals with landslide characteristics. Some progress has been made in interpreting landslide seismic signals, but signal recognition is often hindered by interference from seismic signals generated by other factors (Feng, 2011; Zhao et al., 2015; Fuchs et al., 2018). Several methods have been developed to solve signal noise pollution (Helmstetter and Garambois, 2010; Feng, 2011), but analysis of landslide dynamic characteristics and reconstruction of landslide processes is still subject to errors and inaccuracies. Recently, filtering of seismic signals has been successfully applied to reconstruct dynamic landslide processes, allowing transition stages to be identified that are difficult to derive from field analysis alone (Yan et al., 2020a, 2020b).

Combining seismic signal analysis with dynamic inversion can improve the extraction of landslide dynamic characteristics. Landslide dynamic inversion using long-period seismic records

based on a single-force source model (Kanamori and Given, 1982; Kanamori et al., 1984; Hasegawa and Kanamori, 1987; Dahlen, 1993; Fukao, 1995) and a static point source assumption has been widely adopted to study landslide kinematics (Allstadt, 2013; Ekström and Stark, 2013; Yamada et al., 2013; Hibert et al., 2014, 2015; Moore et al., 2017; Gualtieri and Ekström, 2018; Li et al., 2019b; Sheng et al., 2020; Zhao et al., 2020). Predictive relationships between the maximum inverted forces and sliding volume can be derived from inverted landslide force histories (Ekström and Stark, 2013; Chao et al., 2016). Landslide basal friction is estimated directly using a block model (Brodsky et al., 2003; Allstadt, 2013; Yamada et al., 2013; Zhao et al., 2015; Yu et al., 2020) or obtained from seismic analysis coupled with numerical simulation (Moretti et al., 2012, 2015; Yamada et al., 2016, 2018). Although numerical simulation of landslide dynamic processes has achieved remarkable results, there are issues with each of the following three main approaches. ~~there are issues with each of the two main approaches.~~ The continuous medium approach, including smoothed particle hydrodynamics (SPH) (Pastor et al., 2014), material point method (MPM) (Soga et al., 2016), finite element method (FEM) (Muceku et al., 2016; Wang et al., 2020c), finite volume method (FVM) (Pitman et al., 2003), and finite difference method (FDM) (Shen et al., 2020), is not very effective in describing particle separation and internal fracture of rockslides. The discrete element approach utilizes software such as particle flow code (PFC) (Lo et al., 2011; Zhang et al., 2020a) and DEM solutions (EDEM) (Wang et al., 2020c), but a major issue is low computational efficiency. The thin-layer model, it is based on the thin-layer approximation and depth-averaging of the Navier–Stokes equations without viscosity, but a main issue~~s~~ is low computational accuracy (Moretti et al., 2012, 2015; Yamada et al., 2016, 2018).

MatDEM uses an innovative matrix discrete element method and three-dimensional contact algorithm, which can realize the efficient numerical simulation of millions of particles (Liu et al., 2013, 2017). However, studies utilizing MatDEM mostly determine the correctness of landslide simulation through comparison with post-event landslide characteristics derived from field investigation (Liu et al., 2017), which may not represent dynamic processes. An alternative approach that offers potential is to use seismic signal inversion as the constraint on landslide dynamic process (Yamada et al., 2016, 2018).

In this study, we use long period seismic signal to obtain the dynamic characteristics of Baige landslide, China, which occurred on October 10, 2018 (termed the "10.10" event). By the dynamic inversion results by long period seismic signal which can be used to quality the landslide reconstruction using numerical simulation, and the post-event field investigation and seismic signal analysis, we try to provide an improved characterization of the landslide movement process.~~In this study, we analyze the seismic signal of Baige landslide, China, which occurred on October 10, 2018 (termed the "10.10" event) and obtain the dynamic characteristics of the landslide by dynamic inversion. The inversion results are compared with landslide reconstruction using numerical simulation combined with post-event field investigation, to provide an improved characterization of the landslide movement process.~~

## 2. Study area and data sources

A massive landslide occurred at Baige, on the eastern Qinghai-Tibetan Plateau, China, on October 10, 2018 (Fig. 1). The site is in the Jinsha River suture zone, where the influence of

multiple tectonic movements provides a complicated regional tectonic profile; the main fault structures trend NW, within the Jiangda-Bolo-Jinshajiang fault zone (Deng et al., 2019; Fan et al., 2019b; Xu et al., 2018) (Fig. 2). The landslide can be divided into four areas, shear, main slip, blocking, and deposition, with maximum and average thicknesses of 80 and 50 m, and thins to the sides (Fig. 1c). We used terrain data from Ouyang et al. (2019), comprising a 10 m resolution pre-landslide Digital Elevation Model (DEM) from 2017, and a 5 m resolution post-slide DEM obtained through Unmanned Aerial Vehicle (UAV) photogrammetry in 2018. Based on ~~DEMDigital Elevation Model (~~DEM ~~)~~ differencing, total landslide volume was calculated as c. 1.96~~0~~×~~10~~$^{4}$ $10^{7}$ m$^{3}$. The altitude range of the initiation zone is 3523-3730 m. Most of the rock mass that collapsed from the steep back wall accumulated at an elevation of 3100–3300 m, in an area of gentle slope c. 20–25°.

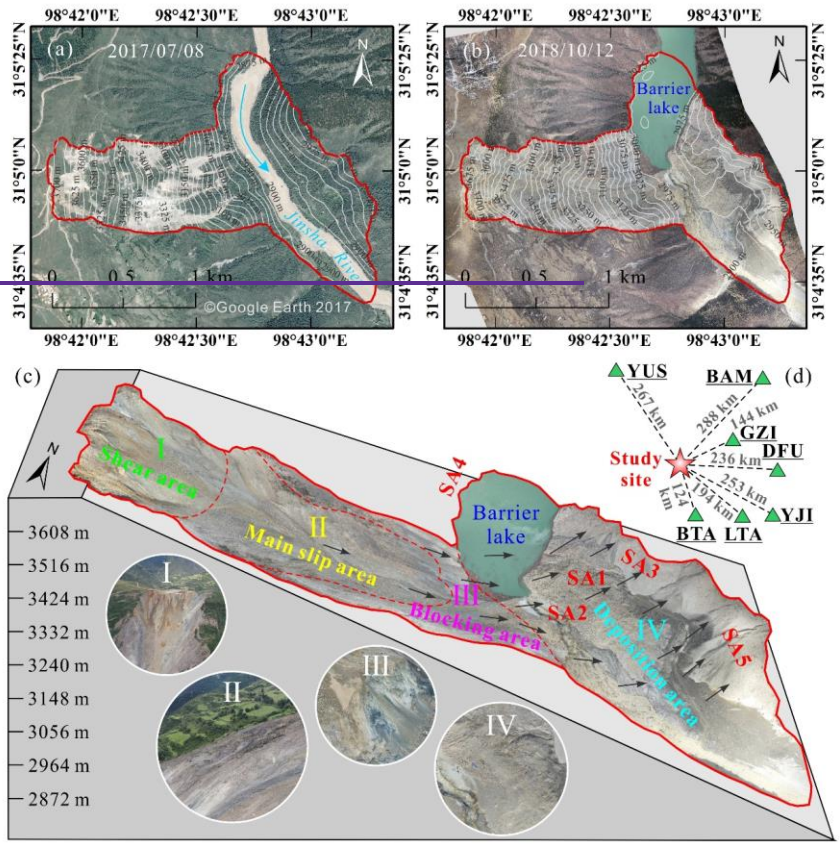
(a) 2017/07/08
(b) 2018/10/12
Barrier lake
Jinsha River
©Google Earth 2017
98°42'0"E
98°42'30"E
98°43'0"E
31°5'25"N
31°5'0"N
31°4'35"N
0 0.5 1 km
N
(c)
I Shear area
II Main slip area
III Blocking area
IV Deposition area
SA1
SA2
SA3
SA4
SA5
Barrier lake
3608 m
3516 m
3424 m
3332 m
3240 m
3148 m
3056 m
2964 m
2872 m
(d)
YUS
BAM
GZI
DFU
YJI
BTA
LTA
Study site
267 km
288 km
144 km
236 km
253 km
194 km
124 km

159

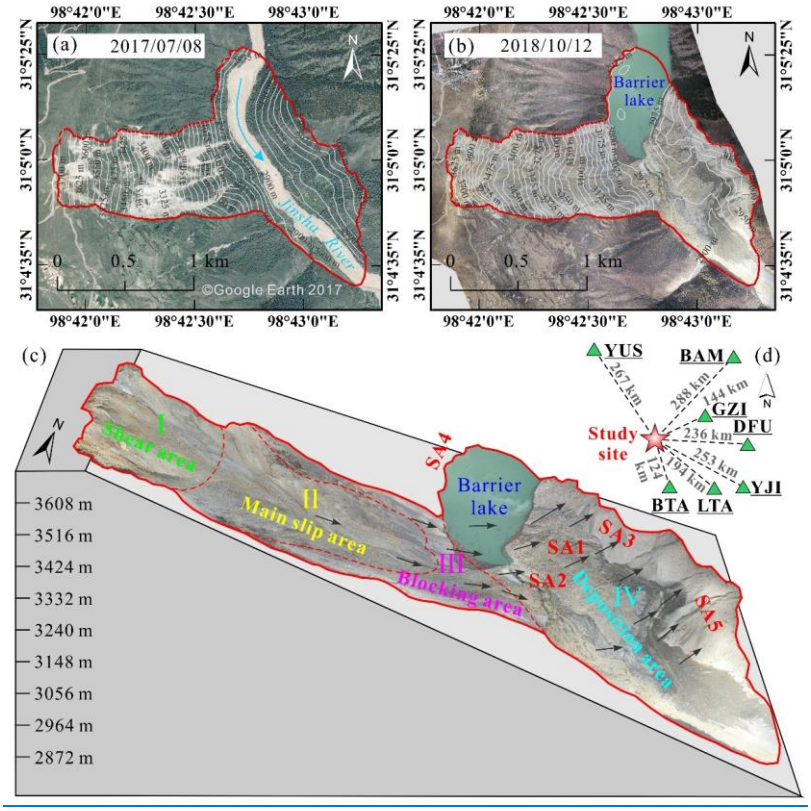


**Fig. 1.** Location of the study area. **(a)** ~~DEM~~DOM of Baige landslide 2017; **(b)** ~~DEM~~DOM of Baige landslide after the 2018 event; **(c)** Schematic cross-section with remote sensing overlay showing key features of the Baige landslide (SA1 and SA2 is a secondary slip zone formed by small fragments at the top of the dam body lose stability; SA3 is the left bank of the river, scoured by landslide debris; SA4 is a small area of the right bank, scoured by landslide debris; SA5 is the downstream left bank, which is affected by the landslide body mix with the sandblasting water); **(d)** Location of the Baige landslide (red star) relative to seismic stations (green triangles) used in the study. The remote sensing image map data of Fig 1.a. is from the © Google Earth 2017, and the data of Fig 1.b. and Fig 1.c. are from the authors' own ~~UAV~~ Unmanned Aerial Vehicle (UAV) photography measurements.

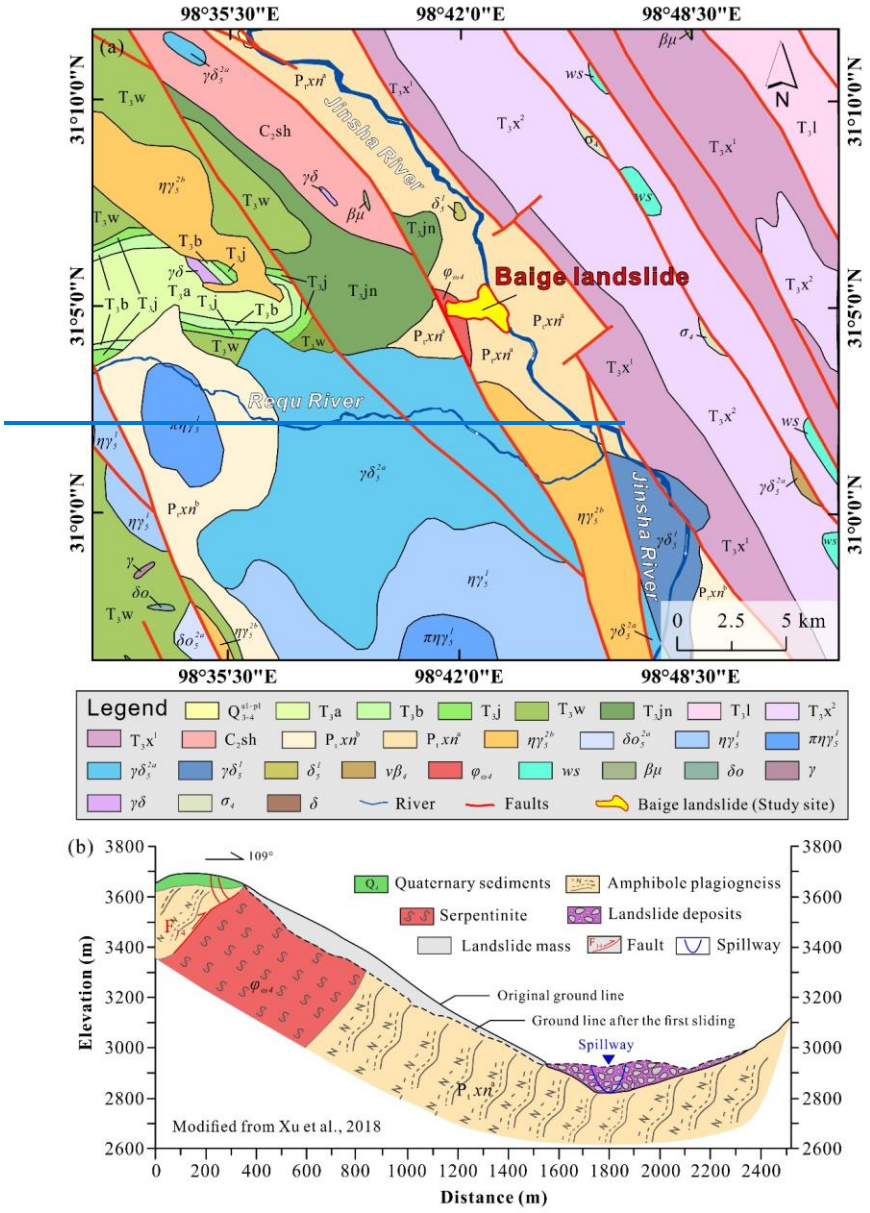
98°35'30"E
98°42'0"E
98°48'30"E
31°10'0"N
31°5'0"N
31°0'0"N
(a)
N
Jinsha River
Baige landslide
Regu River
0 2.5 5 km
Legend
River
Faults
Baige landslide (Study site)
(b)
109°
Quaternary sediments
Amphibole plagiogneiss
Serpentinite
Landslide deposits
Landslide mass
Fault
Spillway
Original ground line
Ground line after the first sliding
Spillway
Modified from Xu et al., 2018
Elevation (m)
Distance (m)

171

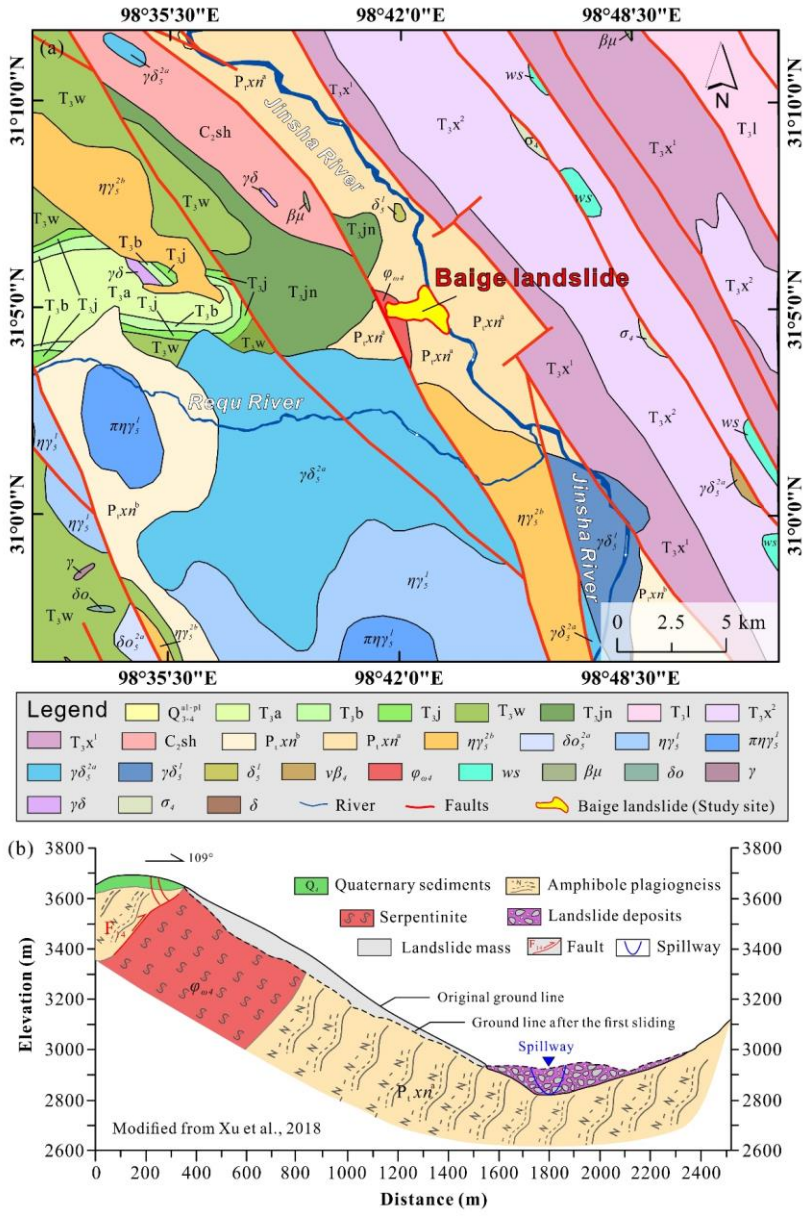


172

173 **Fig. 2.** Geology of the study area. **(a)** Geological map of the Baige landslide area ($Q_{3-4}^{al-pl}$ :

Quaternary Holocene Upper Pleistocene; $T_3a$, $T_3b$, $T_3j$, $T_3w$, $T_3jn$, $T_3l$, $T_3x^2$, $T_3x^1$: Upper Triassic; $C_2sh$: Upper Carboniferous; $P_txn^b$, $P_txn^a$: Proterozoic; $n\gamma_5^{2b}$, $\delta o_5^{2a}$: Yanshan period; $n\gamma_5^1$, $\pi n\gamma_5^1$, $\gamma\delta_5^{2a}$, $\gamma\delta_5^1$, $\delta_5^1$: Indosinian; $v\beta_4$, $\varphi\omega_4$, $\sigma_4$: Variscan; ws: Detached block; $\beta\mu$: Diabase-porphyrite; $\delta o$: Quartz diorite veins; $\gamma$: Granite veins; $\gamma\delta$: Granodiorite dikes; $\delta$: Diorite veins.); **(b)** Cross-section of the landslide showing the geological profile. The geological map data in Figure 2a is from Li et al., 2019a, and the cross-section in Figure 2b is modified from Xu et al., 2018.

We selected broadband seismic signals from seven seismic stations that are distributed around the landslide with adequate azimuth coverage (Fig. 1d) to carry out the analysis. Landslide force history inversion uses long-period seismic waveforms and thus requires that the ambient noise at periods of tens of seconds should be at a low level in the study area. We used the probabilistic power spectral density (PSD) technique (McNamara and Buland, 2004) to characterize the background seismic noise. As illustrated by the PSD of the vertical component for seismic station BTA (Fig. 3), the main seismic energy is distributed between the new high noise model (NHNM) and the new low noise model (NLNM) (Peterson, 1993), indicating that the study area has a relatively good seismic observation environment.

~~We selected broadband seismic signals from seven seismic stations that are distributed around the landslide with good azimuth coverage (Fig. 1d) to carry out the analysis. We used the probabilistic power spectral density (PSD) technique to obtain the background noise level of the selected seismic stations. As illustrated by the PSD of the vertical component for seismic station BTA (Fig. 3), the stations are characterized by low background noise ensuring good data quality.~~

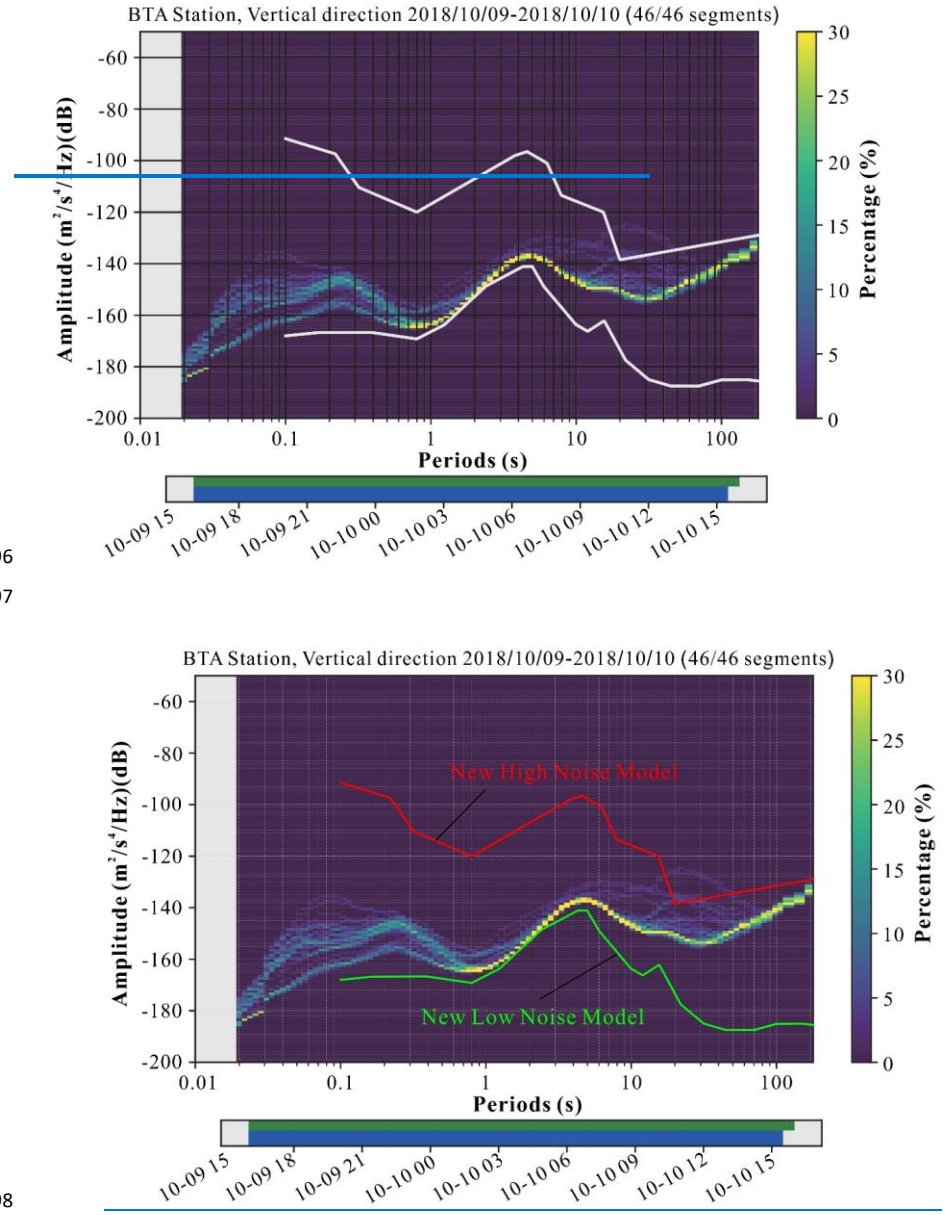


**Fig. 3.** Probabilistic power spectral density of the vertical component at seismic station BTA. White lines in the PSD image are NHNM (the upper one) and NLNM (the lower one). Below the

PSD image is a visualization of the data basis for the calculation. The top row shows data fed into the calculation with green patches representing available data. The bottom row in blue shows the single PSD measurements that go into the histogram.

# 3. Methodology

## 3.1 Seismic data analysis

We used short-time Fourier transform (STFT) and PSD to quantitatively analyze the seismic signals for Baige landslide (Yan et al., 2020a, 2020b).~~We used short-time Fourier transform (STFT) and PSD in the frequency domain to quantitatively analyze the time-frequency characteristics of seismic signals for Baige landslide (Yan et al., 2020a, 2020b).~~ A ~~joint~~ time-frequency domain transform of the seismic signal using STFT allowed information on both the time and frequency domain distributions of the seismic signal to be obtained. The power of each unit of frequency for each frequency band component that corresponds to a specific moment was estimated based on the PSD of the seismic signal in the frequency domain.

## 3.2 Landslide force history inversion

Assuming the landslide source is represented as a series of time-varying forces acting on a static point, synthetic seismograms $u_n(\boldsymbol{x}, t)$ at the seismic station located at $\boldsymbol{x}$ can be computed by convolution of force $f_i(\boldsymbol{x_0}, t_0)$ at $\boldsymbol{x_0}$ with nine-component Green's functions $G_{ni}(\boldsymbol{x}, t; \boldsymbol{x_0}, t_0)$ ( Moretti et al., 2012; Allstadt, 2013; Ekström and Stark, 2013; Yamada et al., 2013; Hibert et al., 2014; Li et al., 2017; Gualtieri and Ekström, 2018),

$$u_n(\boldsymbol{x}, t) = G_{ni}(\boldsymbol{x}, t; \boldsymbol{x_0}, t_0) * f_i(\boldsymbol{x_0}, t_0) \quad (1)$$

where $*$ denotes convolution and bold type face indicates a vector. The Einstein summation convention is assumed in the equation. The convolution can be rewritten as matrix product,

$$\boldsymbol{u}_n = [\boldsymbol{G}_{n1} \quad \boldsymbol{G}_{n2} \quad \boldsymbol{G}_{n3}] \begin{bmatrix} \boldsymbol{f}_1 \\ \boldsymbol{f}_2 \\ \boldsymbol{f}_3 \end{bmatrix} \tag{2}$$

Suppose there are $N$ seismic traces,

$$\begin{bmatrix} \boldsymbol{u}_1 \\ \vdots \\ \boldsymbol{u}_N \end{bmatrix} = \begin{bmatrix} \boldsymbol{G}_{11} & \boldsymbol{G}_{12} & \boldsymbol{G}_{13} \\ \vdots & \vdots & \vdots \\ \boldsymbol{G}_{N1} & \boldsymbol{G}_{N2} & \boldsymbol{G}_{N3} \end{bmatrix} \begin{bmatrix} \boldsymbol{f}_1 \\ \boldsymbol{f}_2 \\ \boldsymbol{f}_3 \end{bmatrix} \tag{3}$$

Use $\boldsymbol{u} = \begin{bmatrix} \boldsymbol{u}_1 \\ \vdots \\ \boldsymbol{u}_N \end{bmatrix}$, $\boldsymbol{G} = \begin{bmatrix} \boldsymbol{G}_{11} & \boldsymbol{G}_{12} & \boldsymbol{G}_{13} \\ \vdots & \vdots & \vdots \\ \boldsymbol{G}_{N1} & \boldsymbol{G}_{N2} & \boldsymbol{G}_{N3} \end{bmatrix}$, and $\boldsymbol{f} = \begin{bmatrix} \boldsymbol{f}_1 \\ \boldsymbol{f}_2 \\ \boldsymbol{f}_3 \end{bmatrix}$, we get the linear forward model

$$\boldsymbol{u} = \boldsymbol{G}\boldsymbol{f} \tag{4}$$

We use $\boldsymbol{u}_o$ to denote observed seismic records and define the 2-norm of the vector difference between $\boldsymbol{u}_o$ and $\boldsymbol{u}$ as an objective function,

$$\boldsymbol{o} = \|\boldsymbol{u} - \boldsymbol{u}_o\|_2 \tag{5}$$

An optimal solution of the forces can be obtained in a least-square sense,

$$\boldsymbol{f} = (\boldsymbol{G}^T\boldsymbol{G})^{-1}\boldsymbol{G}^T\boldsymbol{u}_o \tag{6}$$

The landslide force history can be reconstructed by direct deconvolution of the observed seismograms with Green's functions, which can be readily performed in both time and frequency domains (Allstadt, 2013; Yamada et al., 2013; Li et al., 2017). We calculated Green's Function at the landslide location for each seismic station, using a matrix propagation method (Wang, 1999) and a 1-D layered velocity model from Crust1.0 (https://igppweb.ucsd.edu/~gabi/crust1.html).

Once the landslide force history $\boldsymbol{f}$ was inverted, based on Newton's third law of motion, the forces acting on the sliding mass could be obtained by multiplying the inverted force history by -1 (Kanamori and Given, 1982; Yamada et al., 2013;– Gualtieri and Ekström, 2018). And then the forces acting on the sliding mass can be used to calculate its velocity and displacement

distributions for a given mass (Li et al., 2019c; Yu et al., 2020), or to estimate the sliding mass by minimizing discrepancies with independently derived sliding trajectories (Hibert et al., 2014), using the following equations,

$$\boldsymbol{v} = -\int \frac{\boldsymbol{f}}{m} dt \quad (7)$$

$$\boldsymbol{s} = -\iint \frac{\boldsymbol{f}}{m} dt \quad (8)$$

~~where $*$ denotes convolution and bold type face indicates a vector. The Einstein summation convention is assumed in the equation. The landslide force history can be reconstructed by direct deconvolution of the observed seismograms with Green's functions, which can be readily performed in both time and frequency domains (Allstadt, 2013; Yamada et al., 2013; Li et al., 2017). We calculated Green's Function at the landslide location for each seismic station, using a matrix propagation method (Wang, 1999) and a 1-D layered velocity model from Crust1.0 (https://igppweb.ucsd.edu/~gabi/crust1.html).~~

~~Seismic data were deconvolved with the instrument response to obtain displacement, a 4th-order Butterworth bandpass filter in the frequency band of 0.006–0.2 Hz was then applied, and finally the records were resampled to 0.2 s. Sixteen seismic traces with a signal-to-noise ratio (SNR) larger than 10 dB were selected to carry out the inversion.~~

## 3.3 Numerical modeling

### 3.3.1 Discrete element method

To quantitatively analyze the process of landslide initiation, movement, and accumulation for the "10.10" Baige event, we used MatDEM software, which is based on the matrix discrete element

method, to numerically simulate the landslide (Liu et al., 2017). In the discrete element method, particle movement obeys Newton's second law, and particle velocity and displacement are sequentially updated to simulate the dynamic process of the landslide. In MatDEM, the landslide body is formed by the accumulation and cementation of particles endowed with specific mechanical properties, and the contact and interaction of these particles are defined by the linear elastic bonded model, as shown in Figure 4a. The normal force $F_n$ and tangential force $F_s$ between particles can be expressed by the following formula:

$$F_n = K_n X_n \quad (29)$$

$$F_s = K_s X_s \quad (310)$$

where, $K_n$ is the normal stiffness; $X_n$ is the normal relative displacement between two particles at the contact point; $K_s$ is the tangential stiffness; and $X_s$ is the tangential displacement.

In the normal direction, when the displacement between particles $X_n$ exceeds the fracture displacement $X_b$ the connection between particles is broken and the tension is set as zero. In the tangential direction, spring failure follows the Mohr-Coulomb criterion, and the tangential bond is broken when tangential force exceeds maximum shear force $F_{smax}$, so that only sliding friction $(-\mu_p F_n)$ exists between particles. The maximum normal force $F_{nmax}$ and maximum tangential force that the cementation between particles $F_{smax}$ can withstand is:

$$F_{nmax} = K_n X_b \quad (411)$$

$$F_{smax} = F_{s0} - \mu_p F_n \quad (512)$$

where, $F_{s0}$ is the shear resistance between particles and $\mu_p$ is the friction coefficient between particles.

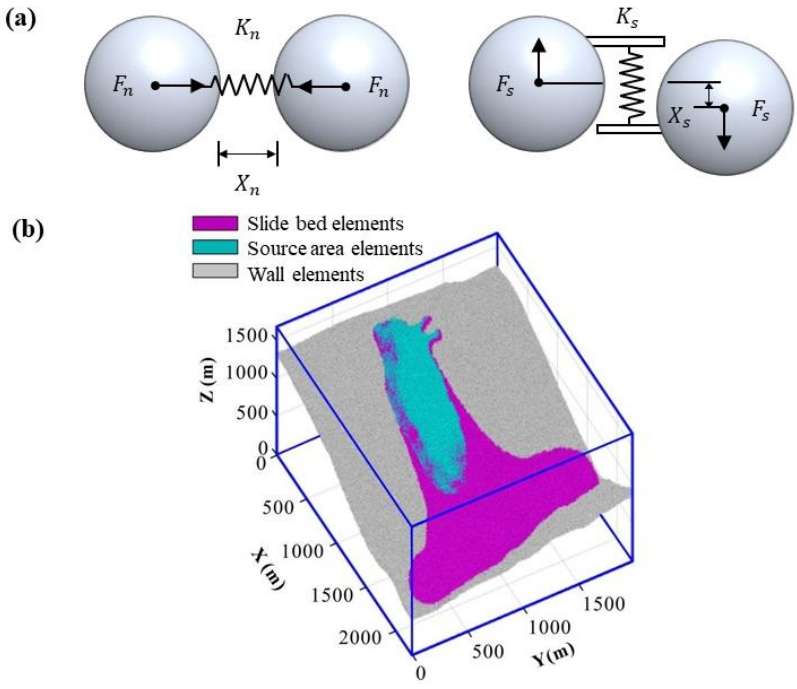


**Fig. 4**. Schematics showing properties of landslide particles and discrete element model. **(a)** Linear elastic bonded model; **(b)** Discrete element model of the Baige landslide (Fan et al., 2019a).

### 3.3.2 Discrete element model of Baige landslide

In MatDEM, the base of the landslide model is constructed of densely packed particles (20 m thick) arranged according to the topography of the slope base. The coordinates of these particles are fixed in the simulation (gray particles in Fig. 4b). The landslide area is constructed by cutting

particles accumulated in the cube model box using the pre- and post- landslide topography. ~~We used terrain data from Ouyang et al. (2019), comprising a 10 m resolution pre-landslide DEM from 2017, and a 5 m resolution post-slide DEM obtained through UAV photogrammetry in 2018.~~ Before starting the simulation, gravity is applied to particles in the sliding source area (blue particles in Fig. 4b) and sedimentary layer (20–80 m thick) (purple particles in Fig. 4b); breaking the connection between particles in the source area allows them to slide down under the action of gravity to simulate landslide initiation. We used a simulation block ~~area~~ of 2270×1980×1680 m, with 582,000 particles comprising 169,000 active cells for simulating landslide movement and 413,000 boundary ~~cells~~ elements to fill the geometry (bottom) and limit the range of activity (side). Average cell size was 5 m and the real-world time 80 s.

"We used the dynamic inverted from seismic signals and deposition characteristics as references for the DEM simulation. Initial macro parameter values, such as Young modulus, Poisson's ratio, were based on results of laboratory tests on Baige landslide materials from Zhou et al. (2019), using the macro and micro conversion formula proposed by Liu et al. (2013) (see Appendix 1 for details), the micro parameters, such as Normal stiffness, Shear stiffness, Breaking displacement, Initial shear resistance, of DEM input can be obtained. As elastic modulus and mechanical properties in laboratory tests are usually higher than those in large-scale rock masses in the field (Darlington et al., 2011; Hencher et al., 2014; Hoek, 2000), Liu et al. (2019) used MatDEM to simulate Xinmo landslide, set Young's modulus and strength to about 40% of the test value, and obtained appropriate simulation results. Therefore, we used 40% of the test value in our simulation.

The second step is to use the geometry of the deposits as a reference to adjusted to obtain reasonable simulation result. For the discrete element method, the geometry of the deposits is affected by the bond strength between particles and the friction coefficient (An et al., 2020), which correspond to the fracture displacement, initial shear force, and friction coefficient between particles in MatDEM. Other parameters, such as normal stiffness and tangential stiffness, remain constant during the simulation. Accuracy of the final landslide accumulation was evaluated by the critical success index (CSI) proposed by Mergili et al. (2017), calculated as:

$$CSI = \frac{TP}{TP + FP + FN} \quad (13)$$

where, TP (true positive) is intersection area from both simulation and filed observation, FN (false negative) is the deposition area observed from field that simulation cannot covered, and FP (false positive) is the additional deposition area from simulation where no deposition is observed from site. CSI ranges between 0 and 1, and the higher the value, the more accurate the simulation; when CSI is 1, the simulated accumulation range coincides with the observed. An et al. (2021) conducted 25 simulations by changing the parameters such as static friction coefficient, thermal weakening friction coefficient and normal bond strength. The results showed that only 8 cases had CSI > 0.6 and the highest CSI was 0.83. In addition, among the 15 groups of results simulated by Mergili et al. (2017), the maximum CSI is 0.59. Therefore, in this study, the criterion is chosen as CSI > 0.6, it can be considered that the simulated accumulation characteristics are basically consistent with the actual situation.

The third step is to use the landslide motion velocity and displacement characteristics inverted by the seismic signal as a reference to back-calibrate parameters that affect the kinematic

characteristics of the landslide, such as friction and average damping coefficients. A flow chart of the method is shown in Fig. 5, and the final values of the parameters are shown in Table 1.

The accuracy of simulated and inversed landslide velocity and displacement was preliminarily evaluated by the relative errors of several key points $\delta$. Then, the variance $S^2$ between the simulated value and the inversion value per second was calculated, and the difference between the two groups of data in the landslide process was analyzed in detail. Related error $\delta$ and variance $S^2$ were calculated as:

$$\delta_x = \frac{X_s - X_i}{X_i} \quad (14)$$

$$S^2 = (X_s - X_i)^2 \quad (15)$$

where, $X_s$ is the simulated value and $X_i$ the inversed value. $X$ can be replaced by landslide duration T, peak velocity $V_{max}$, time when peak velocity achieved $T_{Vmax}$, and peak displacement $D_{max}$.

~~We used the landslide initiation, dynamic, and deposition characteristics inverted from seismic signals as a reference for the discrete element landslide motion simulation. Parameter values were determined according to the accumulation state. For the discrete element method, the range of landslide accumulation is affected by the bond strength between particles and the friction coefficient (An et al., 2020), which correspond to the fracture displacement, initial shear force, and friction coefficient between particles in MatDEM. Other parameters, such as normal stiffness and tangential stiffness, remain constant during the simulation. Parameter values were based on results of laboratory tests on Baige landslide materials in Zhou et al. (2019), using the macro and micro conversion formula.~~. ~~This formula was an experience formula proposed by Liu et al. (2013), its~~

build a bridge from macro parameters to micro parameters. It used to obtain initial parameters of elements. While initial parameters still need to adjusted to obtain reasonable simulation result. As elastic modulus and mechanical properties in laboratory tests are usually higher than those in large-scale rock masses in the field, Liu et al. (2019) used MatDEM to simulate Xinmo landslide, set Young's modulus and strength to about 40% of the test value, and obtained appropriate simulation results. Therefore, refer to it, we used c. 40% of the test value in our simulation. The second step is to use the landslide motion velocity and displacement characteristics inverted by the ground motion signal as a reference to back-determine parameters that affect the kinematic characteristics of the landslide, such as friction and average damping coefficients (a flow chart of the method is shown in Fig. 5, and the final values of the parameters are shown in Table 1). Accuracy of the final landslide accumulation was evaluated by the critical success index (CSI) proposed by Mergili et al. (2017), calculated as:

$$CSI = \frac{TP}{TP + FP + FN} \quad (6)$$

Where, TP (true positive) is where the simulated and observed accumulation areas intersect, FN (false negative) is where the simulated results show no accumulation, but the observed results do, and FP (false positive) is where the simulation result shows accumulation where none is observed. The sum of TP, FP, and FN is the union of the simulation and observation areas. CSI ranges between 0 and 1, and the higher the value, the more accurate the simulation; when CSI is 1, the simulated accumulation range coincides with the observed. In this study, when CSI > 0.6, it can be considered that the simulated accumulation characteristics are basically consistent with the actual situation. This is because it is not easy to obtain the simulation results of CSI > 0.6 in

previous studies. For example, An et al. (2021) conducted 25 simulations by changing the parameters such as static friction coefficient, thermal weakening friction coefficient and normal bond strength. The results showed that only 8 had CSI > 0.6 and the highest CSI was 0.83. Among the 15 groups of results simulated by Mergili et al. (2017), the maximum CSI is 0.59.

The accuracy of simulated and inversed landslide velocity and displacement was preliminarily evaluated by the relative errors of several key points $\delta$. Then, the variance $S^2$ between the simulated value and the inversion value per second was calculated, and the difference between the two groups of data in the landslide process was analyzed in detail. Related error $\delta$ and variance $S^2$ were calculated as:

$$\delta_x = \frac{X_s - X_t}{X_t} \quad (7)$$

$$s^2 = (X_s - X_t)^2 \quad (8)$$

Where, $X_s$ is the simulated value and $X_t$ the inversed value. $X$ can be replaced by landslide duration T, peak velocity $V_{max}$, peak velocity corresponding to time $T_{vmax}$, and peak displacement $D_{max}$.

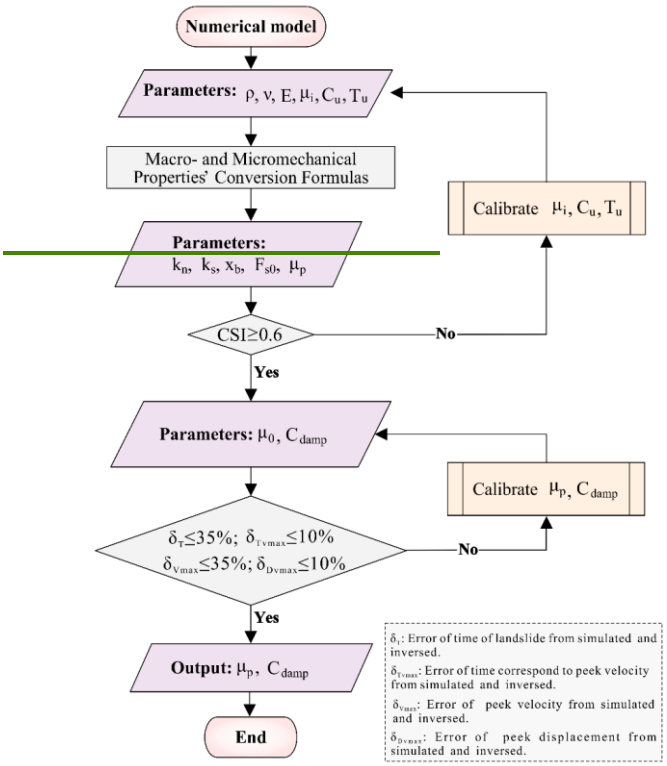
Numerical model
Parameters: ρ, ν, E, μi, Cu, Tu
Macro- and Micromechanical Properties' Conversion Formulas
Parameters: kn, ks, xb, Fs0, μp
Calibrate μi, Cu, Tu
CSI≥0.6
No
Yes
Parameters: μ0, Cdamp
Calibrate μp, Cdamp
δT≤35%; δTvmax≤10%
δVmax≤35%; δDvmax≤10%
No
Yes
Output: μp, Cdamp
End
δT: Error of time of landslide from simulated and inversed.
δTvmax: Error of time correspond to peek velocity from simulated and inversed.
δVmax: Error of peek velocity from simulated and inversed.
δDvmax: Error of peek displacement from simulated and inversed.

383

384

385

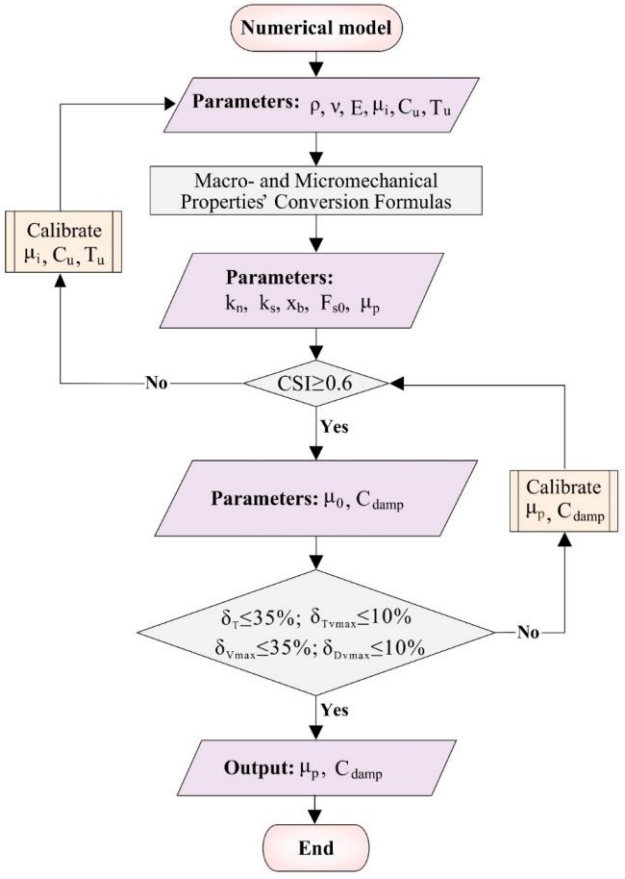


**Fig. 5**. Flowchart of the method of discrete element parameter adjustment based on seismic signal inversion.

**Table 1.** Macro- and micromechanical parameters of Baige landslide material used in the discrete element model.

| Parameter | Value | Reference |
|---|---|---|
| Young modulus $E$ | 20 GPa | Laboratory test (Zhou et al. 2019) |
| Poisson's ratio $\upsilon$ | 0.2 | Laboratory test (Zhou et al. 2019) |
| Uniaxial compressive strength $C_u$ | 30 MPa | Laboratory test & Calibrated |
| Uniaxial tensile strength $T_u$ | 3 MPa | Laboratory test & Calibrated |

| | | |
|---|---|---|
| Internal friction coefficient $\mu_i$ | 0.46 | Laboratory test & Calibrated |
| Density $\rho$ | 2400 kg/m$^3$ | Zhang et al. (2019) |
| Normal stiffness $k_n$ | 486 GN/m | Calculated (Liu et al., 2013) |
| Shear stiffness $k_s$ | 270 GN/m | Calculated (Liu et al., 2013) |
| Breaking displacement $x_b$ | 1.3 mm | Calculated (Liu et al., 2013) |
| Initial shear resistance $F_{s0}$ | 3.28 GN | Calculated (Liu et al., 2013) |
| Intergranular friction coefficient $\mu_p$ | 0.0897 | Calculated & Calibrated |
| Average damping coefficient $C_{damp}$ | 1.06×10$^5$ | Calibrated |

| ~~Parameter~~ | ~~Value~~ |
|---|---|
| ~~Young modulus $E$~~ | ~~20 Gpa~~ |
| ~~Poisson's ratio $\upsilon$~~ | ~~0.2~~ |
| ~~Uniaxial compressive strength $C_u$~~ | ~~30 Mpa~~ |
| ~~Uniaxial tensile strength $T_u$~~ | ~~3 Mpa~~ |
| ~~Internal friction coefficient $\mu_i$~~ | ~~0.46~~ |
| ~~Density $\rho$~~ | ~~2400 kg/m$^3$~~ |
| ~~Normal stiffness $k_n$~~ | ~~486 GN/m~~ |
| ~~Shear stiffness $k_s$~~ | ~~270GN/m~~ |
| ~~Breaking displacement $x_b$~~ | ~~1.3mm~~ |
| ~~Initial shear resistance $F_{s0}$~~ | ~~3.28GN~~ |
| ~~Intergranular friction coefficient $\mu_p$~~ | ~~0.0897~~ |
| ~~Average damping coefficient $C_{damp}$~~ | ~~1.06×10$^5$~~ |

# 4. Results and analysis

## 4.1 Seismic signal analysis

The time-domain velocity curve of the seismic signal generated by the "10.10" Baige landslide is shown in Figure 6. The SNR of the vertical (V) and east (E) components is relative higher, compared with north (N) component, roughly reflecting the main slide direction of

landslide is E and N. Post-event geological survey showed sliding was mainly in south-east-to-south, approximately eastwards.~~The SNR of the vertical (V) and north (N) components is high, and that of the east (E) component is low, reflecting the primary downslope direction of landslide movement; post-event geological survey showed sliding was mainly in a south-east to south direction.~~ The ~~main~~ driving force of the landslide is gravity, and the surface on which the mass slides~~landslide surface~~ is inclined at about 35°, so acceleration~~velocity~~ changes in the longitudinal direction are relatively large, and the SNR of the V component of the landslide signal appears high. During the deposition stage, the main horizontal movement direction of landslide body changed from east-west to north-south, and from north-south limited to east-west limited. The morphology of the landslide channel means that the landslide stage has a large east-west component and a small north-south component, and in the deposition~~accumulation~~ stage, it reverses. This feature is consistent with the high SNR of the N component of the landslide signal and low SNR of the E component.~~During the deposition accumulation stage, the main landslide body moved in an easterly direction, with limited north-south sliding. The morphology of the landslide channel means that the landslide body has a large east-west component and a small north-south component. This feature is consistent with the high SNR of the N component of the landslide signal and low SNR of the E component.~~

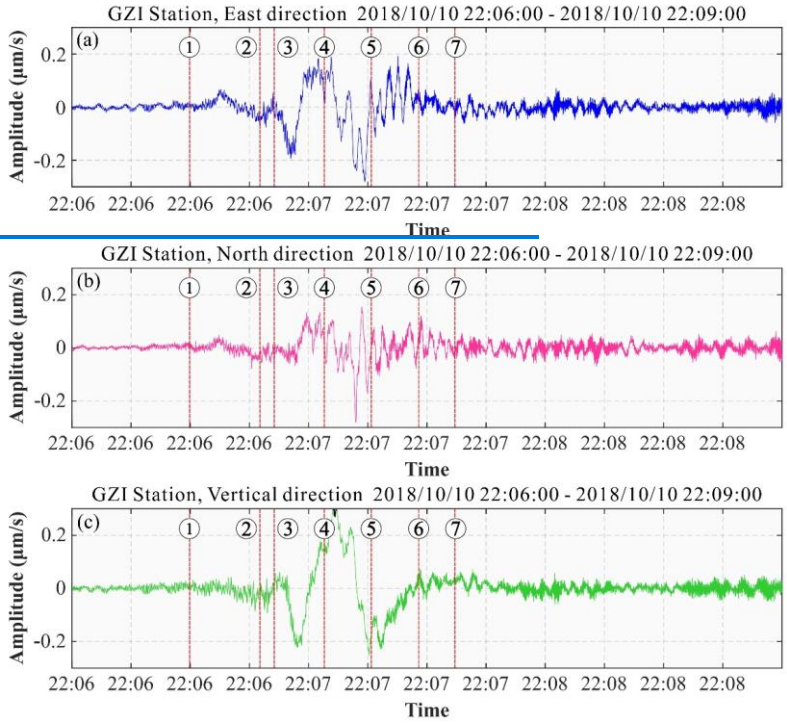
GZI Station, East direction 2018/10/10 22:06:00 - 2018/10/10 22:09:00
(a)
Amplitude (μm/s)
0.2
0
-0.2
① ② ③ ④ ⑤ ⑥ ⑦
22:06 22:06 22:06 22:06 22:07 22:07 22:07 22:07 22:08 22:08 22:08 22:08
Time
GZI Station, North direction 2018/10/10 22:06:00 - 2018/10/10 22:09:00
(b)
Amplitude (μm/s)
0.2
0
-0.2
① ② ③ ④ ⑤ ⑥ ⑦
22:06 22:06 22:06 22:06 22:07 22:07 22:07 22:07 22:08 22:08 22:08 22:08
Time
GZI Station, Vertical direction 2018/10/10 22:06:00 - 2018/10/10 22:09:00
(c)
Amplitude (μm/s)
0.2
0
-0.2
① ② ③ ④ ⑤ ⑥ ⑦
22:06 22:06 22:06 22:06 22:07 22:07 22:07 22:07 22:08 22:08 22:08 22:08
Time

416

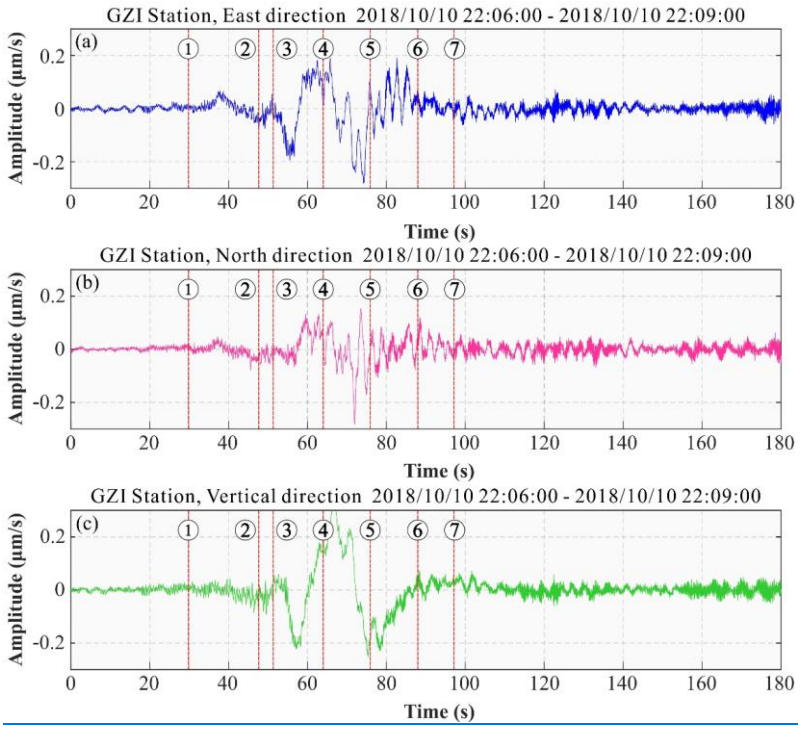


**Fig. 6.** Time-domain acceleration signal (E \N\V direction) of the seismic generated by the Baige landslide at GZI seismic station, showing a relative high signal-to-noise ratio visually but different respectively~~Time-domain velocity curve of the seismic signal generated by the Baige landslide at seismic station GZI (see Figure 1 for location) showing signal-to-noise ratio of the low-frequency components (E\N\V direction)~~.

The sliding distance of the landslide was c. 600 m longitudinally and c. 100 m laterally, while the receiving stations are over 100 km away; as the sliding scale is relatively small relative to the propagation distance, we treated it as a point source. The velocity curve recorded at a seismic station is the velocity of the crustal vibration below the landslide area propagating to the station, and this is roughly determined by velocity and mass of the landslide body. Therefore, characteristics of the landslide downward movement can be obtained by analyzing the velocity

curve recorded at seismic stations. The seismic signal from station GZI (Fig. 6) provides an example to show the general seismic characteristics of the "10.10" Baige landslide. The time-domain acceleration~~velocity~~ curve recorded at GZI determines the start time of the landslide as 22:06 on October 10, 2018 (all times are UTC+8), with a duration of about 76 s between 22:06:39 to 22:07:51. Five points of acceleration~~velocity~~ change are apparent during the landslide process (Fig. 6, Table 2), dividing the event into three phases of acceleration~~velocity~~ and three of deceleration.

Due to seismic wave propagation, the start time determined by the original seismic signal at the station is slightly later than the true time; what's more, the signal is mixed by longitudinal wave that stack with transverse wave, which makes the ending time picked by seismic signal much latter than the actual time. All these make the time of the landslide derived from the original seismic signal would be lagged and longer, compared to the real time~~what's more, the signal is a mixed signal that longitudinal wave stack with transverse wave, which makes the ending time picked by seismic signal. All these make the critical time of the landslide derived from the original seismic signal would be lagged and longer duration time, compared to the reality.~~ ~~, and the signal may also be affected by superimposition of vertical and horizontal waves, which makes the end time lag. So, the critical moments of the landslide derived from the original seismic signal would be lagged, and the duration too long.~~ –A more accurate landslide time can be determined by landslide force history inversion~~inversion~~ as it eliminates the propagation effect. The analysis of the velocity curve recorded at seismic stations~~The analysis here~~ is to help understand the overall characteristics of the landslide and help verify the rationality of the subsequent Green's function stress inversion

results.

**Table 2.** The beginning characteristic stage of the Baige landslide river blocking event picked by seismic signal recorded at GZI station~~Characteristic time of the seismic signal of the Baige landslide river blocking event (recorded at GZI station)~~.

| Landslide stage | | | | | | |
|---|---|---|---|---|---|---|
| Start Time | deceleration | acceleration | deceleration | acceleration | deceleration | End Time |
| 22:06:39 | 22:06:51 | 22:06:54 | 22:07:01 | 22:07:12 | 22:07:27 | 22:07:51 |

The start and end time of sliding is demarcated on the time spectrum of the seismic curve (Fig. 7); strong energy clusters appear around 22:06:39, the intensity begins to decrease at 22:06:54 (UTC+8), and the frequency band narrows and the energy disappears at 22:07:27 (UTC+8). The time spectrum shows the landslide was concentrated between 22:06:40–22:07:01. The frequency is concentrated in the 0–1 Hz range, and the low-frequency component has a high SNR (0–0.2 Hz), which is conducive to dynamic inversion.

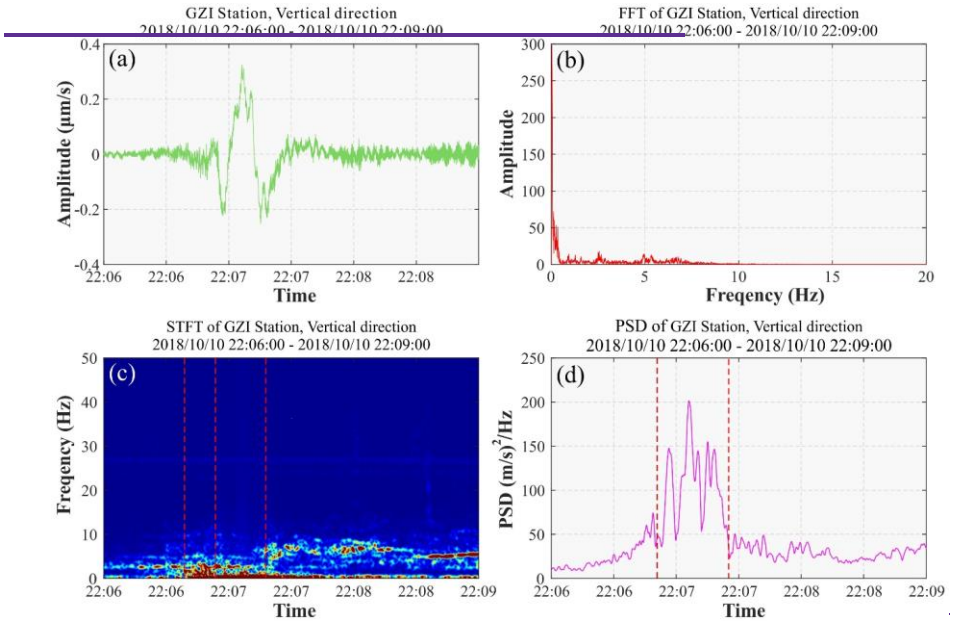

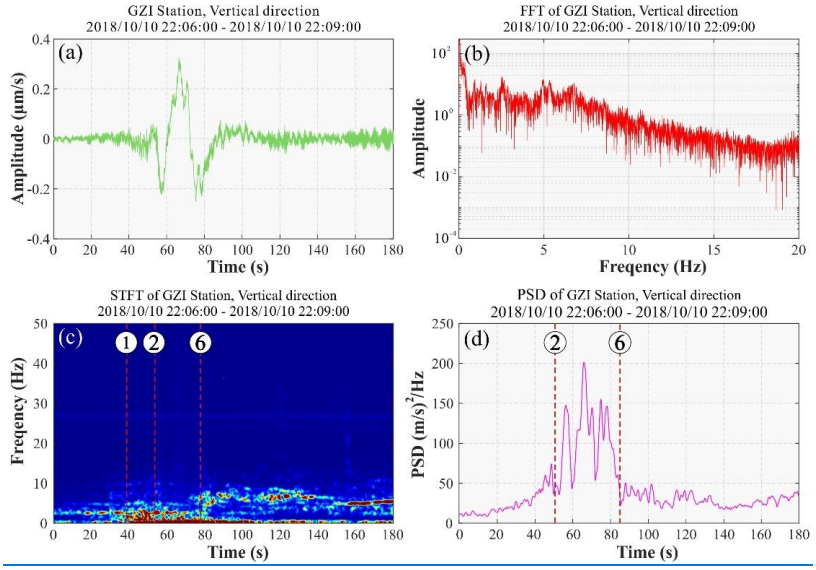


~~**Fig. 7**. Seismic signals of the Baige landslide as recorded at seismic station GZI. **(a)** Vertical seismic signal; **(b)** Frequency spectrum; **(c)** Time-frequency spectrum; and **(d)** Power spectral density (PSD) curve.~~**Fig. 7**. Seismic signals of the Baige landslide as recorded at seismic station GZI. **(a)** Vertical seismic signal; **(b)** Frequency spectrum; **(c)** Time-frequency spectrum and the key times picked frequency from it, that is, start time, 1st acceleration and 3rd deceleration, from left to right respectively; and **(d)** Power spectral density (PSD) curve and the key times picked from it, that is 1st acceleration and 3rd deceleration.

In Figure 7d, the PSD curve is divided into three stages in the longitudinal direction, with the first and third stages corresponding to slow sliding and the second stage to fast sliding. Comparing with the time domain stages (as in Table 2~~);~~ ), the first PSD stage corresponds to the first acceleration and deceleration, the second stage corresponds to the second deceleration, acceleration and third deceleration, and the third stage corresponds to the third deceleration. The PSD curve shows a marked increase in the second stage, indicating rapid downslope sliding, with

multiple large fluctuations indicating rapid changes in landslide movement that are characteristic of the sliding stage.

According to Yan et al (2021), the frequency of landslide hazard seismic signals is usually low (0~5 Hz), and the morphology in the time-frequency domain and time domain presents single-peak or double-peak characteristics, while the frequency of flood or high-density flow seismic signals is usually high (5~50 Hz), and the morphology in the time-frequency domain and time domain mostly presents the characteristics of flat. Combined with this landslide seismic signal has relatively low frequency (0~1 Hz) and the single-peak feature in time and time-frequency characteristics, apparently different from the spectrum (main frequency :15~30 Hz) of the outburst flood signal triggered by the second landslide on October 12, 2018 (An et al, 2021). So, we think there was no flood discharge during the landslide process.~~The low frequency of the landslide seismic signal (0–1 Hz) and the single-peak waveform and time–frequency characteristics suggest there was no flood discharge during the landslide process. Typically, water flow generates a higher frequency (ranging between 0–50 Hz, but mainly 10–40 Hz) (Yan et al., 2017), and the duration and other characteristics are different; also, there is a clear difference from the outburst flood signal on October 12, 2018.~~

## 4.2 Dynamic inversion of landslide

~~The inverted force histories are shown in Fig. 8. The good fit of the synthetic and recorded~~ Seismic data were processed using the following procedure before carrying out the landslide force history inversion. Firstly, they were deconvolved with the instrument response to obtain displacement; then a 4th-order Butterworth bandpass filter in the frequency band of 0.006–0.2 Hz

was then applied; and finally, the records were resampled at a sampling rate of 5 Hz. The processed seismic records have a high signal-to-noise ratio (SNR) as shown in Table ~~1~~3. Sixteen seismic traces with an SNR larger than 10 dB were selected to carry out the inversion.

**Table 3.~~1~~** SNR of seismic signals used in the inversion and CC and VR of the inversion results

| Seismic Station | | SNR | CC | VR |
|---|---|---|---|---|
| BTA | Z | 19.19 | 0.96 | 0.90 |
| | E | 4.28 | 0.56 | 0.28 |
| | N | 8.45 | 0.60 | 0.34 |
| GZI | Z | 29.63 | 0.99 | 0.99 |
| | E | 20.39 | 0.99 | 0.98 |
| | N | 15.29 | 0.97 | 0.94 |
| LTA | Z | 24.67 | 0.99 | 0.98 |
| | E | 7.92 | 0.86 | 0.71 |
| | N | 15.12 | 0.97 | 0.94 |
| DFU | Z | 23.60 | 0.99 | 0.99 |
| | E | 17.58 | 0.99 | 0.98 |
| | N | 5.92 | 0.54 | 0.28 |
| YJI | Z | 22.58 | 0.98 | 0.97 |
| | E | 11.64 | 0.93 | 0.85 |
| | N | 16.75 | 0.95 | 0.90 |
| YUS | Z | 18.05 | 0.94 | 0.89 |
| | E | 19.39 | 0.98 | 0.97 |
| | N | 18.01 | 0.98 | 0.96 |
| BAM | Z | 21.48 | 0.99 | 0.98 |
| | E | 5.86 | 0.74 | 0.53 |
| | N | 10.91 | 0.94 | 0.88 |

The inverted force histories are shown in Fig. 8. The good fit of the synthetic and recorded seismic waveforms in Fig. 9 and the high cross-correlation (CC) and variance reduction (VR) between synthetic and recorded seismograms provided in Table 3 ~~Table 1~~ indicate the high quality of the inversion results. The inverted forces show landslide initiation at 14:05:37.6, with ~61 s duration of the main motion.~~seismic waveforms in Fig. 9 indicates the high quality of the inversion results. The inverted forces show landslide initiation at 14:05:37.6, with ~61 s duration of the main~~

~~motion. Using the empirical relationships of Chao et al. (2016) and Ekström and Stark (2013), the maximum force of $1.37\times10^{11}$ N gives an estimated sliding mass of $5.5\times10^{10}$ kg and $7.4\times10^{10}$ kg, respectively.~~

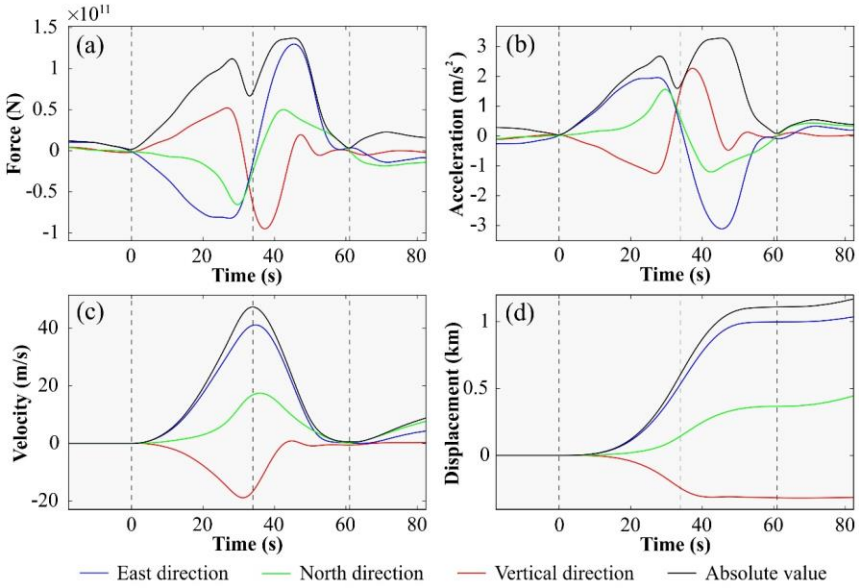


**Fig. 8.** Dynamic inversion used to obtain Baige landslide characteristics**. (a)** Inverted force time history; **(b)** Estimated acceleration distribution over time; **(c)** Reconstructed velocity distribution over time from the inverted landslide force time history; **(d)** Reconstructed displacement distribution over time from the inverted landslide force time history. Corresponding absolute values are shown as ~~dashed~~ black lines. Dashed vertical black lines marked the landslide start and end times (the first and third ones) and the time that the sliding mass reached the maximum speed (the middle one).~~Corresponding absolute values are shown as dashed black lines.~~

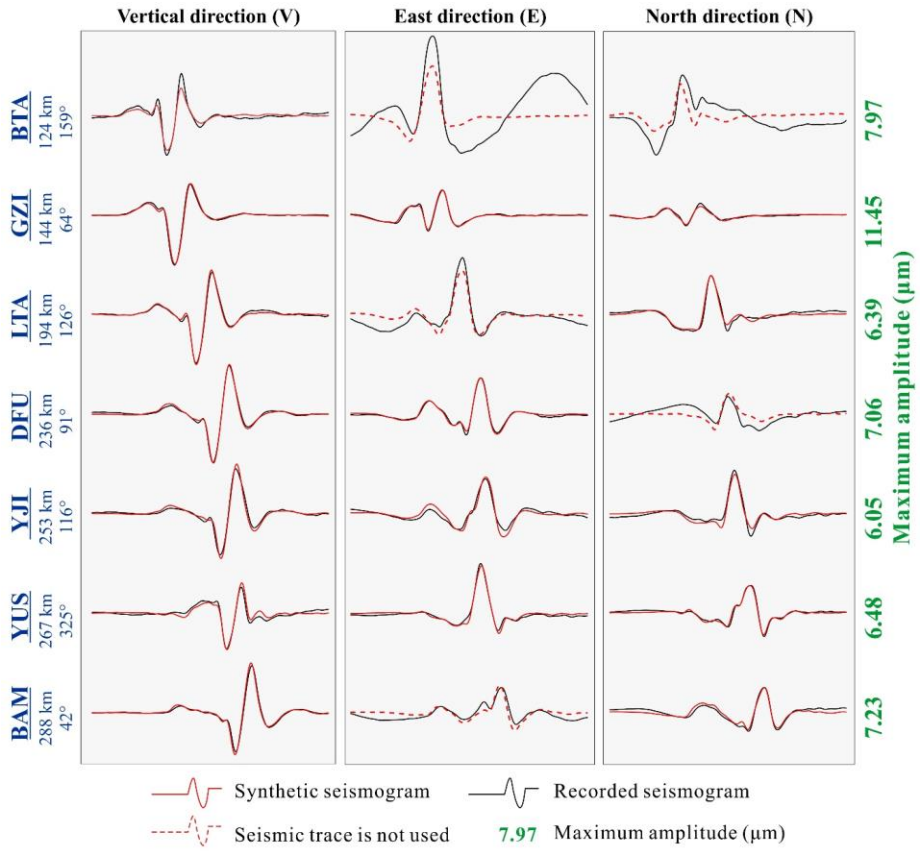


**Fig. 9.** Seismograms of the Baige landslide. Synthetic (red lines) and recorded (black lines) seismograms are compared. Red dotted lines indicate that the seismic trace was not used in the inversion because their SNR is smaller than 10 dB. Station name, distance from study site (km) and azimuth (degree) are given to the left of each trace (see Fig. 1d for locations), and the maximum amplitude of the three components is given in μm to the right.

By comparing the DEMs before and after the event, we determined the mass centers of the source area and the depositional area and subsequently derived the displacement of the center of the sliding mass; then, by minimizing the predicated and actual displacements, wWe ~~adopted the~~

second approach and estimated the sliding mass as c. $4.2\times10^{10}$ kg. The recovered slidinghorizontal and vertical trajectoryies both fit well with the observations, shown in Fig. 10. We used the estimated sliding mass to determine the acceleration and, velocity, and displacement distributions over time (Figs. 8b to 8d).

Based on Newton's third law of motion, the forces acting on the sliding mass are obtained by multiplying the inverted force history by -1 (Kanamori and Given, 1982; Yamada et al., 2013; Gualtieri and Ekström, 2018). We can then use this force to calculate velocity and displacement distributions of the sliding material for a given mass (Li et al., 2019c; Yu et al., 2020), or to estimate the sliding mass by minimizing discrepancies with observed sliding trajectories derived from satellite images (Hibert et al., 2014). We adopted the second approach and estimated the sliding mass as c. $4.2\times10^{10}$ kg. The recovered horizontal and vertical trajectories both fit well with the observations, shown in Fig. 10. We used the estimated sliding mass to determine the acceleration, velocity, and displacement distributions over time (Figs. 8b to 8d).

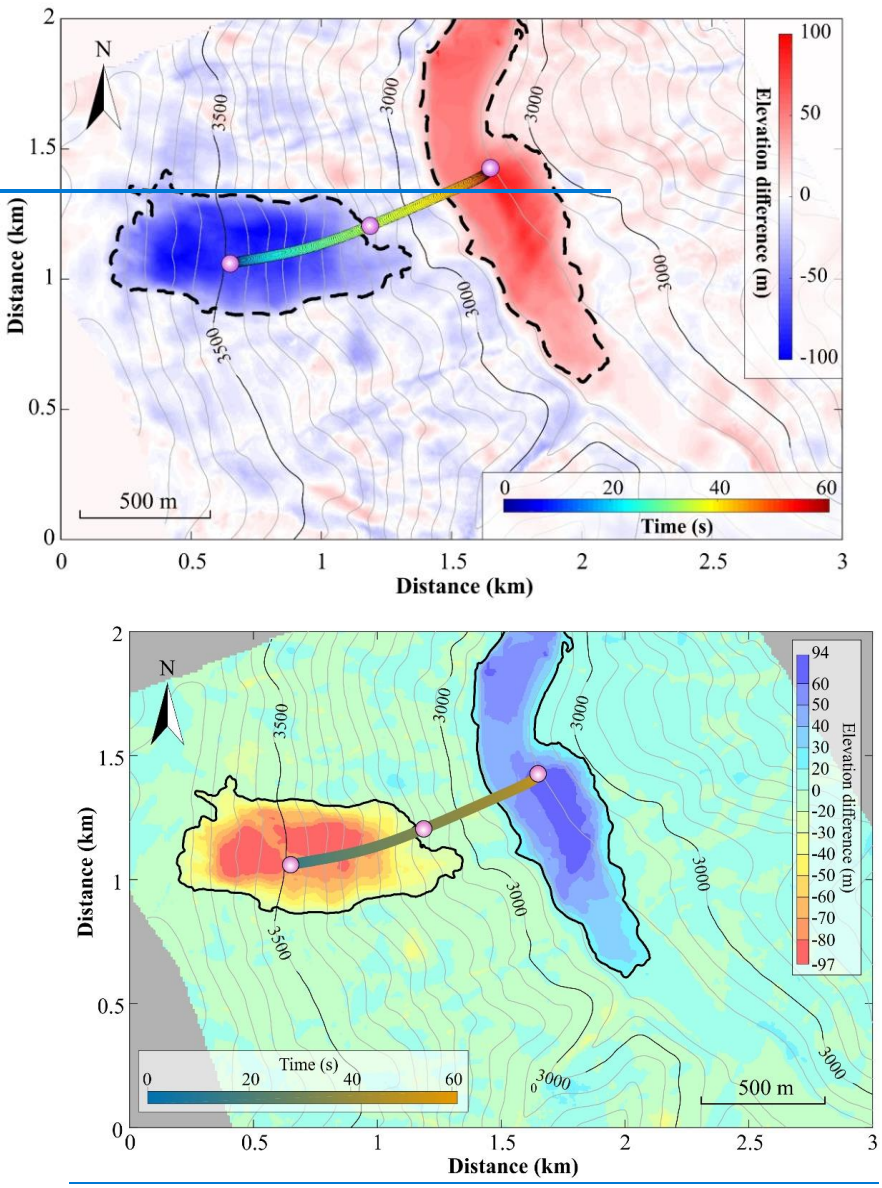


**Fig. 10.** Reconstructed horizontal trajectory of the Baige landslide from the seismic dynamic inversion. The base map is the elevation difference derived from DEMs and the reconstructed trajectory is shown by the colored dots and connecting timeline.

The inversion results show two stages of landslide movement, 34 s of acceleration followed by 27 s of deceleration, which are separated by the vertical dashed black lines in Fig. 8. The sliding mass reached a maximum velocity of 47.4 m/s at the end of the acceleration stage and then rapidly decelerated (Fig. 8c). At c. 50 s, the vertical component shows reverse force and velocity, indicating this was when the main sliding mass traveled over the Jinsha River. The force of the E and V components increases in a nearly linear manner in the first 26 s, but then decreases rapidly~~, indicating that the sliding mass was subject to relatively high frictional force after 26 s~~. The reconstructed horizontal trajectory of the landslide (Fig. 10) indicates that the front of the sliding mass ran up the opposite valley wall after it crossed the Jinsha River~~, which would explain the relatively high frictional force~~.

### 4.3 Numerical modeling results

According to the results of numerical simulation ~~The~~ the movement process of the "10.10" Baige landslide can be divided into three stages: (1) sliding (0–20 s); (2) acceleration when entering the river (20–40 s); and (3) diffusion and accumulation (40–80 s). The velocity distribution through each stage of the simulated landslide is shown in Figure 11.

At the start of the simulation, the connection between particles inside and outside the sliding source area was broken simultaneously to initiate the landslide, which then rapidly fell with a constant (gravitational) acceleration. Due to the small particle friction coefficient (0.0897), simulated average velocity and average displacement growth rate are both higher than that determined in the inversion until 18 s, but their variation trends are similar~~, after which they match~~.

From the variance results, there is little difference between the simulated and inverted landslide velocity and displacement at this stage, as shown in Fig. 12.

In the second stage, the landslide body is moving downwards at a constant acceleration in the simulation, but the inversion shows increased acceleration; so, simulated average velocity and displacement appear to be substantially lower than the inversion. However, the time to reach peak velocity is similar for the simulation (32.8 s) and inversion (32 s). For both velocity and displacement, variance between the inversion and simulation reaches a maximum in this stage, with ~~$R^2$~~ $S^2$ of $2.19\times10^2$ and $2.88\times10^4$. At 40 s, the particles at the front edge of the landslide are stationary due to the obstacle provided by the valley wall/mountain slope on the opposite bank of Jinsha River.

In the third stage, from 40 s, particles in the middle and rear of the landslide body continue to move downwards, spreading and accumulating along the river, with a constant deceleration. After 60 s, the simulated average displacement reaches 1020 m and levels off thereafter, which corresponds well with the inversion. Most particles in the landslide body have accumulated and are stationary at this stage, but a few particles on the trailing edge are still moving. By 80 s, the average velocity tends to 0, showing that landslide movement has ended. The variance of velocity residuals ~~The velocity variance~~ has a secondary peak around 50 s, while the displacement variance decreases gradually. Overall, the simulated accumulation area is relatively small compared with that derived from DEM differencing, although the location of maximum thickness corresponds well (Fig. 13b). The CSI is calculated as 0.65, which suggests the simulation is moderately good.

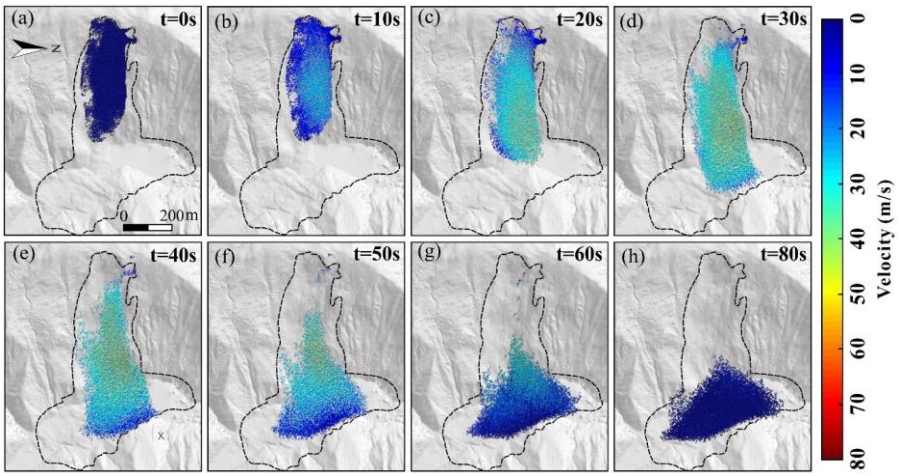


**Fig. 11**. Simulated landslide velocity distribution calculated in MatDEM. **(a)** t =0 s; **(b)** t =10 s; **(c)** t =20 s; **(d)** t =30 s; **(e)** t =40 s; **(f)** t =50 s; **(g)** t =60 s; **(h)** t =80 s. The digital terrain model (DTM) data of Fig 11. are from the authors' own UAV photography measurements.

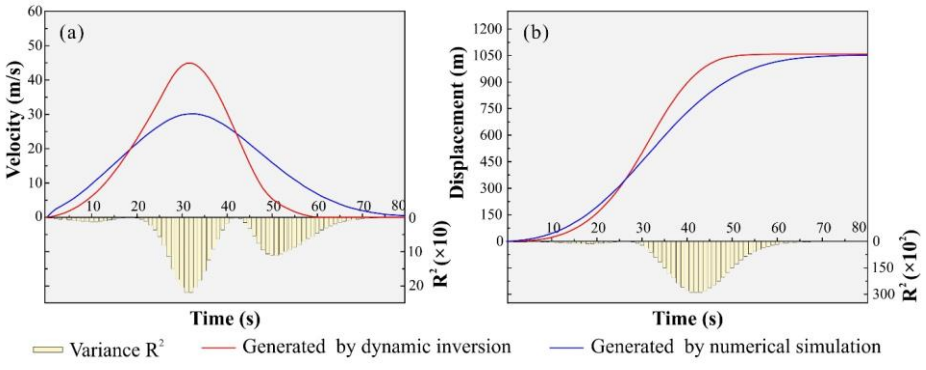

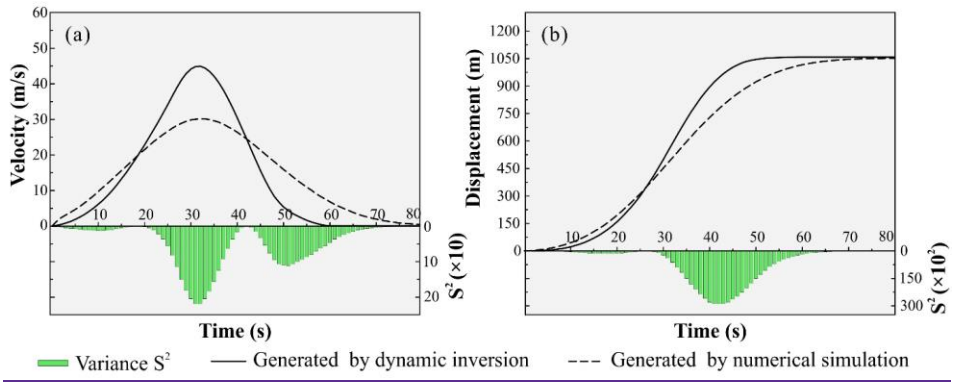


**Fig. 12**. Comparison of landslide characteristics simulated using discrete element model with inversion results. **(a)** Average velocity; **(b)** Average displacement.

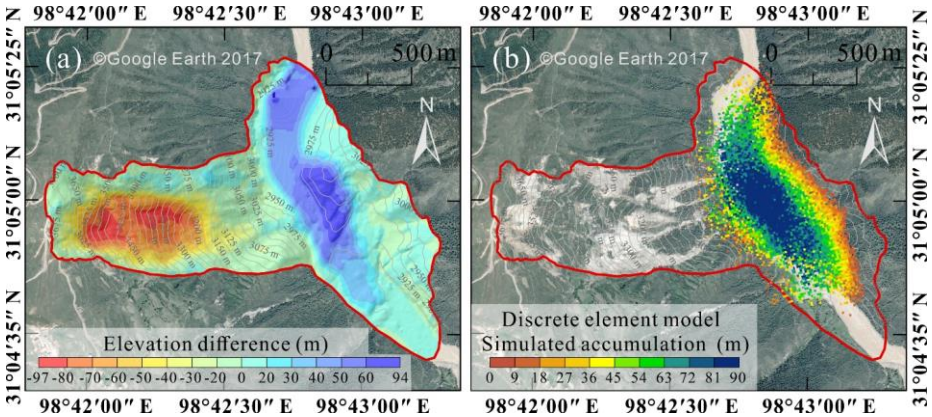


**Fig. 13**. Comparison of elevation change associated with the Baige landslide. **(a)** Estimated from pre- and post-failure topography; **(b)** Calculated using the discrete element model. The remote sensing image map data of Fig 13.a. and b. are from the © Google Earth 2017.

# 5. Discussion

## 5.1 Field observation and dynamic inversion

~~Our estimates of the sliding mass from inversion data, based on the empirical relationships~~

Using the empirical relationships of Chao et al. (2016) and Ekström and Stark (2013), the

maximum inverted force of $1.37\times10^{11}$ N gives an estimated sliding mass of $5.5\times10^{10}$ kg and $7.4\times10^{10}$ kg, respectively, which are about 1.32 and 1.77 times of our estimation of about $4.2\times10^{10}$ kg from landslide force inversion. This is not surprising as we used a different frequency band in our inversion (0.006–0.2 Hz) than the two studies (e.g., Ekström and Stark (2013) used the frequency band 0.0067 – 0.0286 Hz(35–150 s)). Previous work has shown that, for the same event, use of different frequency bands produces landslide force histories of different amplitudes (Hibert et al., 2014; Moore et al., 2017; Zhang et al., 2020b). As a comparison, we performed inversion in the frequency band 0.0067 – 0.0286 Hz, which gave a maximum force of $1.03\times10^{11}$ N and sliding mass estimates of $4.20\times10^{10}$ kg and $5.60\times10^{10}$ kg that are more consistent with our estimation. Since the frequency bands we used are close at the low-frequency end, the kinematic parameters estimated from both inversion results are essentially similar in their characterization of overall landslide motion. We used the frequency band including relatively higher frequency energy (up to 0.2 Hz) in the inversion to allow finer scale characteristics of the forces and landslide motion to be analyzed (Zhao et al., 2015), such as the near-linear increase of the vertical component force in the first 26 s and subsequent abrupt decrease.

~~from Chao et al. (2016) and Ekström and Stark (2013), are about 1.77 and 1.32 times that derived from pre- and post-event DEM differencing. This is not surprising as we used a different frequency band in our inversion (0.006–0.2 Hz) than the two studies (e.g., Ekström and Stark (2013) used the period band 35–150 s). Previous work has shown that, for the same event, use of different frequency bands produces landslide force histories of different amplitudes (Hibert et al., 2014; Moore et al., 2017; Zhang et al., 2020b). As a comparison, we performed inversion in the period~~

band 35–150 s, which gave a maximum force of $1.03\times10^{11}$ N and sliding mass estimates of $5.60\times10^{10}$ kg and $4.20\times10^{10}$ kg that are more consistent with the DEM result. Since the frequency bands we used are close at the low-frequency end, the kinematic parameters estimated from both inversion results are essentially similar in their characterization of overall landslide motion. We used the period band including relatively higher frequency energy (up to 0.2 Hz) in the inversion to allow finer scale characteristics of the forces and landslide motion to be analyzed (Zhao et al., 2015), such as the near-linear increase of the vertical component force in the first 26 s and subsequent abrupt decrease.

## 5.2 Link with numerical modeling

The numerical simulation combining signal inversion and field data more realistically reflects the landslide process than that based on field data alone. Differencing of pre- and post-landslide terrain data is commonly used to calibrate discrete element simulations; however, it is a recognized limitation that this method does not inform on whether the landslide process is correctly modeled. Different combinations of discrete element parameters may produce very similar superposition results even the motion processes differ. In this study, the simulation is calibrated by the accumulation characteristics, and then the landslide movement process is further constrained by the inversion of the seismic signal. The final simulation results produced CSI of 0.65, $\delta T_{vmax}$ of 2.5%, $\delta D_{max}$ ~~$_{max}$~~ of 0.6%, $\delta T$ of 33.3%, $\delta V_{max}$ of 33.3% ($\delta T_{vmax}$: error of time corresponds to peek velocity from simulated and inversed; $\delta D_{max}$: error of peek displacement from simulated and inversed; $\delta T$: error of time of landslide from simulated and inversed; $\delta V_{max}$: error of peek velocity from simulated and inversed), indicating they reflect the whole process of movement and

accumulation well, overcoming the limitations of traditional methods.

Differences in the kinetic characteristics of different landslide phases between the numerical simulation and inversion are highlighted using analysis of variance (Fig. 12). For example, the inversion results simulate the sliding stage (0–20 s) best, the diffusion and deposition~~accumulation~~ stage (40–80 s) second, and the acceleration stage (20–40 s) least. The good simulation of the sliding stage may be due to the fracture zone not yet being completely detached, so landslide movement is dominated by sliding of the whole body, which the theoretical assumption in the inversion approach. In the acceleration stage of large-scale landslides, friction between the sliding rock and soil and the base generates heat, which causes thermal compression and fluidization, leading to soil weakening (Wang et al., 2017, 2018). Reduction in the friction coefficient means the landslide moves faster, however, this factor is not considered in the current inversion model, so it ~~overestimates~~ under-estimates peak velocity (Fig. 12). Despite the differences in kinematics, the simulation is essentially consistent with reality in terms of accumulation and movement characteristics.

### 5.3 Reconstruction of landslide process

The Baige landslide has been the focus of much previous research (Xu et al., 2018; Deng et al., 2019; Fan et al., 2019a; Ouyang et al., 2019; Zhang et al., 2019; Wang et al., 2020a), however, this study is the first analysis that couples seismic signal analysis, dynamic inversion, and numerical simulation. Our approach of multi-method mutual verification effectively reduces the inherent ambiguity of each method, and multi-method analysis improves the rationality and reliability of the results. Based on the characteristics of the “10.10” Baige landslide derived from

our seismic signal inversion and discrete element model simulation analysis, we have developed a generic model of landslide dynamics (Figure 14). Our findings show the landslide was triggered by detachment of the weathered layer with severe top fault segmentation and the landslide process comprised four stages: initiation, main slip, blocking, and deposition, as outlined below.

1. Initiation stage (Fig. 14a): The fracture zone on the upper part of the first-level platform loses stability and slides down under the action of gravity. Landslide debris is hindered by friction on the surface of the main sliding zone, so the landslide body moves relatively slowly. Increasing debris accumulates on the first-level platform and the lower main sliding area, which increases instability of the weathered layer, and other debris continues to fall downslope. The surface weathering layer of the main sliding area starts to slide, and the landslide body forms after the first fracture in the fracture development zone. Cascading from the initial fracture, continuous fracturing and sliding of the shear zone causes the landslide body to gradually increase; sliding of the top surface of the main sliding zone increases the scale of the landslide body. Downward sliding gradually accelerates as the landslide body increases, but friction in the main sliding area then acts to decelerate the mass; the deceleration process can be seen in the signal recorded at seismic station GZI (Fig. 7). As a result, acceleration increases slowly over c. 10 s; this is evident in both the inversion and numerical simulation results.

2. Main slip stage (Fig. 14b): The main sliding area gradually loses stability and slides rapidly under the control of structural surfaces formed by weathering; the landslide body passes through the main sliding area and enters the wide and gentle second level platform where resistance is relatively high. After crossing the second level platform, the landslide enters the slip resistance

693 zone where the degree of weathering is relatively weak, so the scouring action of the landslide
694 body drives resistance. The effect of both sliding and anti-slip zones on the landslide body is
695 relatively weak and is characterized well by the seismic signal in the time domain and the inverted
696 acceleration curve. The initial sliding stage of the main sliding zone is reflected in the gradually
697 increasing acceleration that peaks when the landslide body reaches the second level platform, and
698 then decreases. When acceleration is approximately zero, the front part of the landslide has entered
699 the river, and velocity of the landslide body peaks; the timing of maximum velocity in the inversion
700 and simulation is consistent, at 32 s and 34 s, respectively (Fig. 12a).

701 3. Blocking stage (Crawling up the opposite valley wall) (Fig. 14c): After passing through the
702 anti-slip area, the landslide detaches at high speed at an altitude of c. 2950 m and loses support of
703 the ground surface. Part of the landslide body accumulates in the river and part hits the opposite
704 (left) bank of the Jinsha River at a high speed and crawls upwards against the valley slope. During
705 the upward movement, landslide debris spreads upstream and downstream, scouring the left bank
706 of the river (SA3 in Fig. 1c) and a small area of the right bank (SA4 in Fig. 1c). Landslide debris
707 reaches a maximum elevation of 3045 m on the opposite slope, then slides downslope under the
708 action of gravity, forming debris strips like the scratches found on the sliding surface. Some debris
709 remains on the relatively gentle slope of the left bank. The main feature of this process is that the
710 action of gravity changes the force of the landslide body from dynamic to resistance; this is well
711 reflected in the time-domain seismic curve and inversion results (Fig. 8), where the acceleration
712 switches rapidly from increasing to decreasing over c. 10 s. As the upward crawling situation was
713 not considered in the model design, the numerical simulation failed to describe the process.

4. Deposition stage (Falling back and accumulation) (Fig. 14d): Debris rapidly falls back down under the action of gravity, colliding with debris in the traction area of the river channel and interacting with stream flow to form a jet stream. Some finer particles in the landslide body mix with the sandblasting water to form a water-sand jet that discharges diagonally across the river, toward the downstream left bank (SA5 in Fig. 1c) and upstream right bank (SA4 in Fig. 1c). Most of the detrital material stops moving and is deposited in the river channel, forming a barrier dam that starts to pond water. Under gravity and the action of water flow, small fragments at the top of the dam body lose stability and form a secondary slip zone (SA1 and SA2 in Fig. 1c) that becomes a drainage channel. The acceleration change during this downturn is roughly the same as the change trend of the main sliding phase. Acceleration first gradually increases and then decreases to zero before entering the deceleration phase. The seismic curve in the time domain and the inverted acceleration curve both characterize this process well, and the inversion results give a duration of c. 10 s.

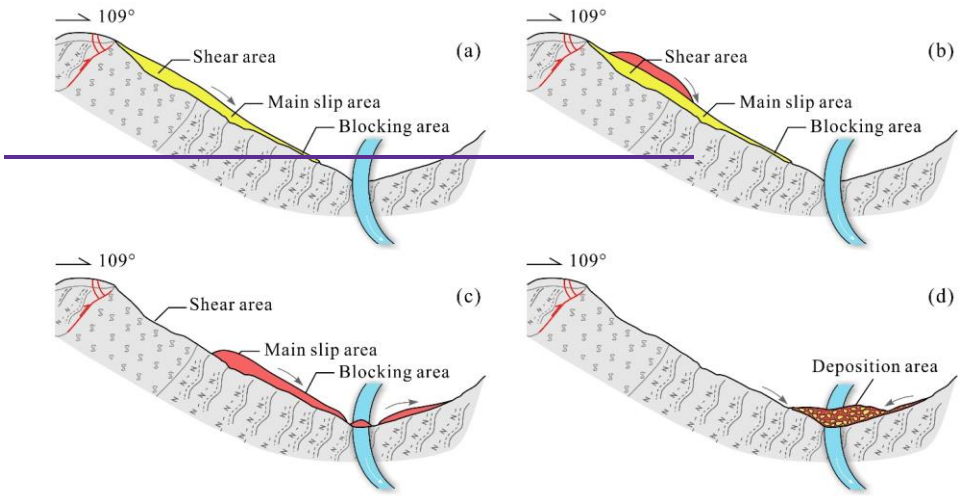
109°
Shear area
(a)
Main slip area
Blocking area
109°
Shear area
(b)
Main slip area
Blocking area
109°
Shear area
(c)
Main slip area
Blocking area
109°
(d)
Deposition area

727

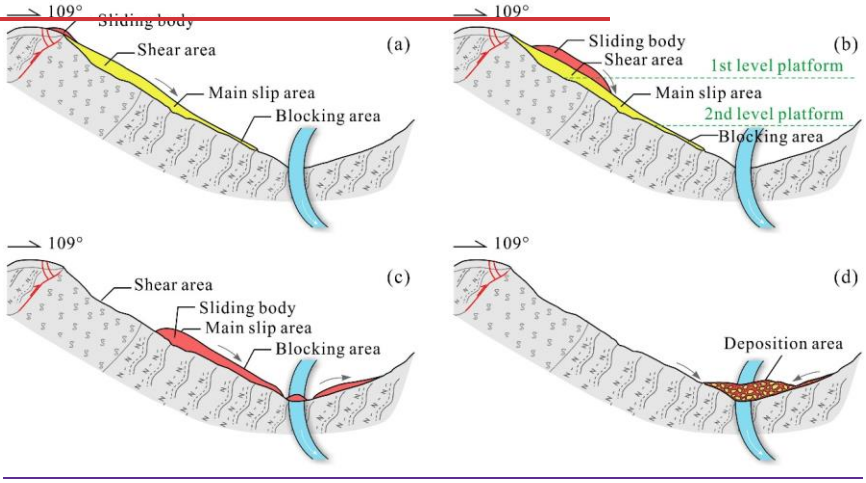
109°
Sliding body
Shear area
(a)
Main slip area
Blocking area
109°
Sliding body
Shear area
(b)
1st level platform
Main slip area
2nd level platform
Blocking area
109°
Shear area
(c)
Sliding body
Main slip area
Blocking area
109°
(d)
Deposition area

728

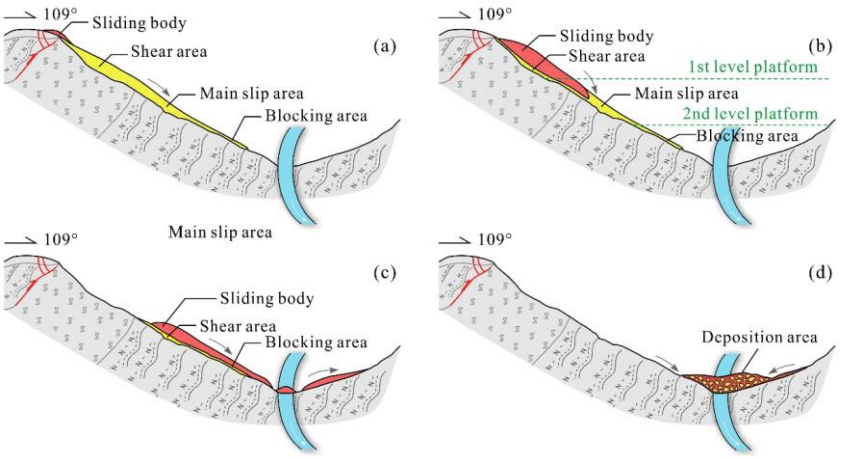


**Fig. 14.** Schematic diagram of the Baige landslide model. **(a)** Stage 1 –initiation; **(b)** Stage 2 – main slip; **(c)** Stage 3 – crawling up against the slope (blocking); **(d)** Stage 4 – falling back and accumulation (deposition).

## 5.4 Research contribution

Post-event geological survey can examine depositional characteristics of the landslide and weathering and fracture conditions of rocks in the slide source area, which provides some information for understanding landslide causal processes. The seismic signal provides some information on landslide evolution, with the low-frequency component reflecting the overall movement trend of the landslide and the high-frequency component reflecting detailed characteristics of the movement process. Experienced researchers can reconstruct the landslide process using a combination of geological survey and seismic signal analysis. However, the propagation effect of the stratum means that the seismic signal does not completely correspond to landslide movement and may generate false images, as well as confounding precise determination of landslide start time and duration.

Landslide dynamic inversion based on the long-wavelength information of the seismic signal eliminates the propagation effect which allows the dynamic parameter curve of the landslide to be obtained, giving a relatively accurate determination of landslide start and end time and event

duration. The dynamic inversion result reflects the change process of the overall movement trend of the landslide (the low-frequency trend) and can be used to verify the results of combined geological survey and seismic signal analysis. The low-frequency (0~0.2 Hz) component of dynamic parameters, as provided by dynamic inversion, can guide the all band frequency motion, concentrating the high frequency (>0.2 Hz) movement, analysis of the landslide process, which helps to reduce ambiguity. ~~The low-frequency component of dynamic parameters, as provided by dynamic inversion, can guide the high-frequency motion analysis of the landslide process, which helps to reduce ambiguity.~~

The accuracy of numerical simulation results depends on scientific models and accurate parameters. When static parameters such as pre- and post-landslide topography are used to select parameters and constrain results of numerical simulation, there are often multiple solutions. The accuracy of the landslide dynamic with time evolution process will not be determined using only the calibration of the accretion morphology, because different velocities, evolutionary processes may produce similar accretionary landforms (An et al. 2021; Mergili et al. 2017), especially for mega-landslides like Baige, which occur next to deep-incised valleys.~~Dynamic inversion results can dynamically and quantitatively constrain the dynamic parameters and increase the credibility of the numerical simulation to produce highly effective simulation of the landslide process.~~ Compared with the study of An et al. (2021), which mainly focuses on force time history inversion, we further added the velocity and displacement characteristics retrieved from seismic signals to conduct dynamic quantitative constraints on dynamic parameters and improve the credibility of numerical simulation, so as to carry out efficient simulation of landslide process. The improved simulation allows in-depth analysis of frequency motion characteristics of the landslide, such as speed change, characteristics of each stage, etc. These characteristics can also be used to verify and optimize the landslide process to improve analysis results.

Each of the three methods has disadvantages which may lead to errors and ambiguities in analyzing landslides. However, the combined use and mutual verification of the different methods can effectively avoid ambiguity and improve the reasonableness of results.

## 6. Conclusions

In this study, we use on-site geological survey, landslide seismic signal analysis, dynamic inversion, and numerical simulation to provides a comprehensive analysis of "10.10" Baige landslide. We used short-time Fourier transform (STFT) and PSD to analyze the seismic signals for Baige landslide. We then reconstructed the landslide force history by direct deconvolution of the observed seismograms with Green's functions. We then developed a method that use seismic inversion to constrain and calibrate the numerical input parameters using DEM. With the assessment of numerical simulation, the dynamic process of "10.10" Baige landslide was then analysed. Nevertheless, several key issues, such as friction weaking, base entrainment, particle breakage, are not considered in the DEM, which leads the difference between simulation and inversion, should be considered in future research.~~The "10.10" Baige landslide was triggered by instability of highly weathered serpentinite at the top, with severe fracture and cutting, which led to downward sliding of the severely weathered gneiss group in the lower part along the bottom sliding surface. Part of the front edge of the landslide was detached on the bottom of the slip area, blocking area, and some other parts, over the Jinsha Rvier, slid up against its opposite slope, and then~~Part of the front edge of the landslide was detached on the left bank of the Jinsha River, slid up against the opposite slope on the right bank, and then slid down and deposited in the river together with the main landslide body. The accumulated mass blocked the river to impound a barrier lake.

~~**Our study has demonstrated that combing with on site geological survey, landslide seismic signal analysis, dynamic inversion, and numerical simulation provides a comprehensive and accurate method for studying the landslide process.** On site geological survey combined with seismic signal analysis can approximate the overall process of landslide evolution, but the results are influenced by the analyst's experience and professional background,~~

~~with a relatively high level of training required. Dynamic inversion provides data on changes in dynamic parameters during the landslide process, which enables the analyst to intuitively analyze the physical parameters of the landslide process. However, dynamic inversion results lack the high frequency component of the landslide process; a combination of seismic signal analysis and numerical simulation results is more comprehensive. Dynamic parameter inversion can eliminate the propagation effect of seismic waves and can accurately determine the start and end time of the landslide. The low-frequency changes of dynamic parameters obtained by the inversion inform analysis of the landslide process and calibrate numerical simulation results. Reasonable and accurate numerical simulation results can dynamically visualize the landslide process, which helps in-depth understanding and verification of the landslide process. In short, available methods for landslide analysis each have advantages and disadvantages, but in combination the inherent ambiguities of each method are reduced and the accuracy of landslide process results is increased.~~

# 7. Appendix 1

## Macro and Micro Conversion Formula of Discrete Element Model

There is an analytical solution between the macro and micromechanical parameters of the tightly packed discrete element model, that is, the conversion formula proposed by Liu et al. (2013). For the linear elastic model, there are five micromechanical parameters, that is, the normal stiffness ($K_n$), shear stiffness ($K_s$), breaking displacement ($X_b$), shear resistance ($F_{s0}$), coefficient of friction ($\mu_p$) can be defined by Young's modulus ($E$), Poisson's ratio ($v$), tensile strength ($T_u$), compressive strength ($C_u$) and coefficient of intrinsic friction ($\mu_i$). The conversion formulas are as follows:

$$K_n = \frac{E}{\sqrt{3}(1-2v)(1+v)} \quad \text{(A1)}$$

$$K_s = \frac{E(1-4v)}{\sqrt{3}(1-2v)(1+v)} \quad \text{(A2)}$$

$$X_b = \frac{2K_n + K_s}{2\sqrt{3}K_n(K_n+K_s)} T_u d \quad \text{(A3)}$$

$$F_{s0} = (\frac{1}{4} - \frac{\sqrt{3}}{4}\mu_p)C_u d \quad \text{(A4)}$$

$$\mu_p = \frac{-3\sqrt{3} + \sqrt{3}I}{3 + 3I}, I = [(1 + \mu_i)^{0.5} + \mu_i]^2 \quad \text{(A5)}$$

where $K_n$ and $K_s$ are the normal and shear stiffness of the particle, respectively; $E$ is Young's modulus; $v$ is Poisson's ratio; $X_b$ is breaking displacement; $T_u$ is uniaxial tensile strength; $d$ is particle diameter; $F_{s0}$ is initial shear resistance; $\mu_p$ is intergranular friction coefficient; $C_u$ is uniaxial compressive strength; $\mu_i$ is internal friction coefficient.

## ~~7.~~8. Acknowledgements

This study was financially supported by the National Natural Science Foundation of China (grant nos. 42120104002, 41901008, U21A2008), the Second Tibetan Plateau Scientific Expedition and Research Program (STEP) (grant no. 2019QZKK0906), and the Fundamental Research Funds for the Project of Science & Technology Department of Sichuan Province (grant no. 2020YFH0085).

The probabilistic power spectral densities (PSD) are calculated and plotted using ObsPy (https://docs.obspy.org/).

## Data availability

All raw data can be provided by the corresponding authors upon request.

## Author contributions

The authors of this manuscript entitled "Combining seismic signal dynamic inversion and numerical modeling improves landslide process reconstruction" are Yan Yan, Yifei Cui, Xinghui Huang, Wengang Zhang, Shuyao Yin, Jiaojiao Zhou, Sheng Hu. Yan Yan is the first author, is responsible for most of the work and paper writing in this research. Yifei Cui is the second author and the corresponding author, is responsible for the processing and verification of the article data.

Xinghui Huang is the third author and is responsible for the production of the article figures. Wengang Zhang is the fourth author and is responsible for checking the overall logical structure of the article. Shuyao Yin is responsible for the numerical simulations. Jiaojiao Zhou is the seventh author and is responsible for drawing the tables. Sheng Hu is responsible for reviewing and editing the manuscript.

## Competing interests

The authors declare that they have no conflict of interest.

## ~~8.~~9. References


Allstadt, K.: Extracting source characteristics and dynamics of the August 2010 Mount M eager landslide from broadband seismograms, J. Geophys. Res.-Earth, 118, 1472–149 0, https://doi.org/10.1002/jgrf.20110, 2013.

An, H. C., Ouyang, C. J., Zhao, C., and Zhao, W.: Landslide dynamic process and para meter sensitivity analysis by discrete element method: the case of Turnoff Creek roc k avalanche, J. Mt. Sci., 17, 1581-1595, https://doi.org/10.1007/s11629020-5993-7, 20 20.

An, H. C, Ouyang, C. J, Zhou, S.: Dynamic process analysis of the Baige landslide by t he combination of DEM and long-period seismic waves., Landslides, 18, 1625-1639, https://doi.org/10.1007/s10346-020-01595-0, 2021.

Brodsky, E. E., Gordeev, E., and Kanamori, H.: Landslide basal friction as measured by seismic waves, Geophys. Res. Lett., 30, 2236, https://doi.org/10.1029/2003GL018485, 2003.

Chao, W. A., Zhao, L., Chen, S. C., Wu, Y. M., Chen, C. H., and Huang, H. H.: Seis mology-based early identification of dam-formation landquake events, Sci. Rep., 6, 1 9259, https://doi.org/10.1038/srep19259, 2016.

Chao, W. A., Wu, Y. M., Zhao, L., Chen, H., Chen, Y. G., Chang, J. M., and Lin, C. M.: A first near real-time seismology-based landquake monitoring system, Sci. Rep., 7, 43510, https://doi.org/10.1038/srep43510, 2017.

Chen, C. H., Chao, W. A., Wu, Y. M., Zhao, L., Chen, Y. G., Ho, W. Y., Lin, T. L., Kuo, K. H., and Chang, J. M.: A seismological study of landquakes using a real-ti me broad-band seismic network, Geophys. J. Int., 194, 885-898, http://doi.org/10.1093 /gji/ggt121, 2013.

Dahlen, F. A.: Single-force representation of shallow landslide sources, B. Seismol. Soc. Am., 83, 130–143, http://doi.org/10.1785/BSSA0830010130, 1993.

881 Dammeier, F., Moore, J. R., Hammer, C., Haslinger, F., and Loew, S.: Automatic detecti
882 on of alpine rockslides in continuous seismic data using hidden Markov models, J.
883 Geophys. Res.-Earth, 121, 351-371, http://doi.org/10.1002/2015jf003647, 2016.
884 Darlington, W.J., Ranjith, P.G., and Choi, S.K.: The Effect of Specimen Size on Strength
885 and Other Properties in Laboratory Testing of Rock and Rock-Like Cementitious Br
886 ittle Materials, Rock Mech Rock Eng, 44, 513, https://doi.org/10.1007/s00603-011-016
887 1-6, 2011.
888 Deng, J. J., Gao, Y. J., Yu, Z. Q., and Xie, H. P.: Analysis on the Formation Mechanis
889 m and Process of Baige Landslides Damming the Upper Reach of Jinsha River,Chin
890 a, Adv. Eng. Sci., 51, 9-16, http://doi.org/10.15961/j.jsuese.201801438, 2019.(In Chine
891 se)
892 Ekström, G., and Stark, C. P.: Simple scaling of catastrophic landslide dynamics, Science.
893 339, 1416–1419. https://doi.org/10.1126/science.1232887, 2013.
894 Fan, X., Yang, F., Subramanian, S. S., Xu, Q., Feng, Z., Mavrouli, O., Peng, M., Ouyan
895 g, C., Jansen, D., and Huang, R.: Prediction of a multi-hazard chain by an integrate
896 d numerical simulation approach: the Baige landslide, Jinsha River, China, Landslide
897 s, 17, 147-164, http://doi.org/10.1007/s10346-019-01313-5, 2019a.
898 Fan, X., Xu, Q., Liu, J., Subramanian, S. S., He, C., Zhu, X., and Zhou, L.: Successful
899 early warning and emergency response of a disastrous rockslide in Guizhou province,
900 China, Landslides, 16, 2445–2457, https://doi.org/10.1007/s10346-019-01269-6, 2019b.
901 Favreau, P., Mangeney, A., Lucas, A., Crosta, G., and Bouchut, F.: Numerical modeling
902 of landquakes, Geophys. Res. Lett., 37, L15305, http://doi.org/10.1029/2010gl043512,
903 2010.
904 Feng, Z.: The seismic signatures of the 2009 Shiaolin landslide in Taiwan, Nat. Hazards
905 Earth Syst. Sci., 11, 1559-1569, http://doi.org/10.5194/nhess-11-1559-2011, 2011.
906 Feng, Z. Y., Lo, C. M., and Lin, Q. F.: The characteristics of the seismic signals induce
907 d by landslides using a coupling of discrete element and finite difference methods,
908 Landslides, 14, 661-674, http://doi.org/10.1007/s10346-016-0714-6, 2016.
909 Froude, M. J., and Petley, D. N.: Global fatal landslide occurrence from 2004 to 2016,
910 Nat. Hazards Earth Syst. Sci., 18, 2161-2181, http://doi.org/10.5194/nhess-18-2161-201
911 8, 2018.
912 Fuchs, F., Lenhardt, W., and Bokelmann, G.: Seismic detection of rockslides at regional
913 scale: examples from the Eastern Alps and feasibility of kurtosis-based event locatio
914 n, Earth Surf. Dynam., 6, 955-970, http://doi.org/10.5194/esurf-6-955-2018, 2018.
915 Fukao, Y.: Single-force representation of earthquakes due to landslides or the collapse of
916 caverns, Geophys. J. Int., 122, 243–248, https://doi.org/10.1111/j.1365-246X.1995.tb03
917 551.x, 1995.
918 Gualtieri, L., and Ekström, G.: Broad-band seismic analysis and modeling of the 2015 T
919 aan Fjord, Alaska landslide using Instaseis, Geophys. J. Int., 213, 1912–1923, https://
920 doi.org/10.1093/gji/ggy086, 2018.

Hasegawa, H. S., and Kanamori, H.: Source mechanism of the magnitude 7.2 Grand Banks earthquake of November 1929: Double couple or submarine landslide?, B. Seismol. Soc. Am., 77, 1984–2004, 1987.

Helmstetter, A., and Garambois, S.: Seismic monitoring of Séchilienne rockslide (French Alps): Analysis of seismic signals and their correlation with rainfall, J. Geophys. Res., 115, F03016, http://doi.org/10.1029/2009jf001532, 2010.

Hencher, S. R., Richards, L. R.: Assessing the Shear Strength of Rock Discontinuities at Laboratory and Field Scales, Rock Mech Rock Eng, 48, 883-905, https://doi.org/10.1007/s00603-014-0633-6, 2014.

Hibert, C., Ekström, G., and Stark, C. P.: Dynamics of the Bingham Canyon Mine landslides from seismic signal analysis, Geophys. Res. Lett., 41, 4535–4541, https://doi.org/10.1002/2014GL060592, 2014.

Hibert, C., Stark, C. P., and Ekström, G.: Dynamics of the Oso-Steelhead landslide from broadband seismic analysis, Nat. Hazards Earth Syst. Sci., 15, 1265–1273, https://doi.org/10.5194/nhess-15-1265-2015, 2015.

Hoek E.: Rock engineering course notes by Evert Hoek. http://www.rocscience.com/education/hoeks_corner, 2000.

Jiang, Y., Wang, G., and Kamai, T.: Fast shear behavior of granular materials in ring-shear tests and implications for rapid landslides, Acta Geotech., 12, 645-655, http://doi.org/10.1007/s11440-016-0508-y, 2016.

Kääb, A., Leinss, S., Gilbert, A., Bühler, Y., Gascoin, S., Evans, S. G., Bartelt, P., Berthier, E., Brun, F., Chao, W. A., Farinotti, D., Gimbert, F., Guo, W., Huggel, C., Kargel, J.S., Leonard, G.J., Tian, L., Treichler, D., and Yao, T.: Massive collapse of two glaciers in western Tibet in 2016 after surge-like instability, Nat. Geosci., 11, 114–120, https://doi.org/10.1038/s41561-017-0039-7, 2018.

Kanamori, H., and Given, J.W.: Analysis of long-period seismic waves excited by the May 18, 1980, eruption of Mount St. Helens—A terrestrial monopole?, J. Geophys. Res.-Sol. Ea., 87, 5422–5432, https://doi.org/10.1029/JB087iB07p05422, 1982.

Kanamori, H., Given, J. W., and Lay, T.: Analysis of seismic body waves excited by the Mount St. Helens eruption of May 18, 1980, J. Geophys. Res.-Sol. Ea., 89, 1856–1866, https://doi.org/10.1029/JB089iB03p01856, 1984.

Kao, H., Kan, C. W., Chen, R. Y., Chang, C. H., Rosenberger, A., Shin, T .C., Leu, P. L., Kuo, K. W., and Liang, W. T.: Locating, monitoring, and characterizing typhoon-induced landslides with real-time seismic signals, Landslides, 9, 557-563, http://doi.org/10.1007/s10346-012-0322-z, 2012.

Li, C. Y., Wang, X. C., He, C. Z., Wu, X., Kong, Z. Y., and Li, X. L. China National Digital Geological Map (Public Version at 1:200 000 Scale) Spatial Database(V1). Development and Research Center of China Geological Survey; China Geological Survey[producer], 1957. National Geological Archives of China [distributor], 2019-06-30. https://doi.org/10.23650/data.A.2019.NGA120157.K1.1.1.V1, 2019a.

Li, W., Chen, Y., Liu, F., Yang, H., Liu, J., and Fu, B.: Chain-style landslide hazardous process: Constraints from seismic signals analysis of the 2017 Xinmo landslide, SW China, J. Geophys. Res.-Sol. Ea., 124, 2025–2037, https://doi.org/10.1029/2018JB016433, 2019b.

Li, Z., Huang, X., Xu, Q., Yu, D., Fan, J., and Qiao, X.: Dynamics of the Wulong landslide revealed by broadband seismic records, Earth, Planets Space, 69, 27, https://doi.org/10.1186/s40623-017-0610-x, 2017.

Li, Z., Huang, X., Yu, D., Su, J., and Xu, Q.: Broadband-seismic analysis of a massive landslide in southwestern China: Dynamics and fragmentation implications, Geomorphology, 336, 31–39. https://doi.org/10.1016/j.geomorph.2019.03.024, 2019c.

Liu, C., Pollard, D. D., and Shi, B.: Analytical solutions and numerical tests of elastic and failure behaviors of close-packed lattice for brittle rocks and crystals, J. Geophys. Res.-Sol. Ea., 118, 71-82, https://doi.org/10.1029/2012JB009615, 2013.

Liu, C., Xu, Q., Shi, B., Deng, S., and Zhu, H.: Mechanical properties and energy conversion of 3D close-packed lattice model for brittle rocks, Comput. Geosci., 103, 12-20, https://doi.org/10.1016/j.cageo.2017.03.00, 2017.

Liu, C., Fan, X., Zhu, C., and Shi, B.: Discrete element modeling and simulation of 3-Dimensional large-scale landslide-Taking Xinmocun landslide as an example-, J. Eng. Geol, 27, 1362-1370-, https://doi.org/10.13544/j.cnki.jeg.2018-234, 2019. (In Chinese)

Lo, C. M., Lin, M. L., Tang, C. L., and Hu, J. C.: A kinematic model of the Hsiaolin landslide calibrated to the morphology of the landslide deposit, Eng. Geol., 123, 22-39, https://doi.org/10.1016/j.enggeo.2011.07.002, 2011.

McNamara, D.E., Buland, R.P., 2004. Ambient Noise Levels in the Continental United States. Bull. Seismol. Soc. Am. 94, 1517–1527. https://doi.org/10.1785/012003001

Mergili, M., Fischer, J. T., Krenn, J., and Pudasaini, S. P.: r. avaflow v1, an advanced open-source computational framework for the propagation and interaction of two-phase mass flows, Geosci. Model Dev, 10, 553-569, https://doi.org/10.5194/gmd-10-553-2017, 2017.

Mergili, M., Emmer, A., Juřicová A., Cochachin, A., Fischer, J. T., Huggel, C., and Pudasaini, S. P.: How well can we simulate complex hydro-geomorphic process chains? The 2012 multi-lake outburst flood in the Santa Cruz Valley (Cordillera Blanca, Perú)-, Earth Surf Process Landf, 43, 1373-1389-, https://doi.org/10.1002/esp.4318, 2017.

Moore, J. R., Pankow, K. L., Ford, S. R., Koper, K. D., Hale, J. M., Aaron, J., and Larsen, C.F.: Dynamics of the Bingham Canyon rock avalanches (Utah, USA) resolved from topographic, seismic, and infrasound data, J. Geophys. Res.-Earth, 122, 615–640, https://doi.org/10.1002/2016JF004036, 2017.

Moretti, L., Mangeney, A., Capdeville, Y., Stutzmann, E., Huggel, C., Schneider, D., and Bouchut, F.: Numerical modeling of the Mount Steller landslide flow history and of the generated long period seismic waves, Geophys. Res. Lett., 39, L16402, https://doi.org/10.1029/2012GL052511, 2012.

Moretti, L., Allstadt, K., Mangeney, A., Capdeville, Y., Stutzmann, E., and Bouchut, F.: Numerical modeling of the Mount Meager landslide constrained by its force history derived from seismic data, J. Geophys. Res.-Sol. Ea., 120, 2579–2599, https://doi.org/10.1002/2014JB011426, 2015.

Muceku, Y., Korini, O., and Kuriqi, A.: Geotechnical analysis of hill's slopes areas in h eritage town of Berati, Albania. Period. Polytech., Civ. Eng. 60, 61-73, https://doi.org/10.3311/PPci.7752, 2016.

Ouyang, C. J., An, H. C., Zhou, S., Wang, Z. W., Su, P. C., and Wang, D. P.: Insights from the failure and dynamic characteristics of two sequential landslides at Baige v illage along the Jinsha River, China, Landslides, 16, 1397-1414, https://doi.org/10.1007/s10346-019-01177-9, 2019.

Pastor, M., Blanc, T., Haddad, B., Petrone, S., Sanchez, M. M., Drempetic, V., Issler, D., Crosta, G. B., Cascini, L., Sorbino, G., and Cuomo, S.: Application of a SPH depth integrated model to landslide run-out analysis, Landslides, 11, 793812, https://doi.org/10.1007/s10346-014-0484-y, 2014.

Peterson, J.R., 1993. Observations and modeling of seismic background noise, U.S. Geological Survey Open-File Report 93-322. https://doi.org/10.3133/ofr93322.

Pitman, E. B., Nichita, C. C., Patra, A., Bauer, A., Sheridan, M., and Bursik, M.: Computing granular avalanches and landslides, Phys. Fluids., 15, 3638-3646, ,https://doi.org/10.1063/1.1614253, 2003.

Sakals, M. E., Geertsema, M., Schwab, J. W., and Foord, V. N.: The Todagin Creek landslide of October 3, 2006, Northwest British Columbia, Canada, Landslides, 9, 107-115, http://doi.org/10.1007/s10346-011-0273-9, 2011.

Schöpa, A., Chao, W. A., Lipovsky, B. P., Hovius, N., White, R. S., Green, R. G., and Turowski, J. M.: Dynamics of the Askja caldera July 2014 landslide, Iceland, from seismic signal analysis: precursor, motion and aftermath, Earth Surf. Dynam., 6, 467–485, https://doi.org/10.5194/esurf-6-467-2018, 2018.

Shen, W., Li, T., Li, P., and Lei, Y.: Numerical assessment for the efficiencies of check dams in debris flow gullies: A case study, Comput. Geotech., 122, 103541, https://doi.org/10.1016/j.compgeo.2020.103541, 2020.

Sheng, M., Chu, R., Wang, Y., and Wang, Q.: Inversion of source mechanisms for single-force events using broadband waveforms, Seismol. Res. Lett., 91, 1820–1830, https://doi.org/10.1785/0220190349, 2020.

Soga, K., Alonso, E., Yerro, A., Kumar, K., and Bandara, S.: Trends in large-deformation analysis of landslide mass movements with particular emphasis on the material point method, Géotechnique, 66, 1-26, https://doi.org/10.1680/jgeot.15.lm.005, 2016.

Walter, M., Arnhardt, C., and Joswig, M.: Seismic monitoring of rockfalls, slide quakes, and fissure development at the Super-Sauze mudslide, French Alps, Eng. Geol., 128, 12-22, http://doi.org/10.1016/j.enggeo.2011.11.002, 2012.

Wang, L. Q., Yin, Y. P., Huang, B. L., and Dai, Z. W.: Damage evolution and stability analysis of the Jianchuandong Dangerous Rock Mass in the Three Gorges Reservoir Area, Eng. Geol., 265, 105439, http://dx.doi.org/10.1016/j.enggeo.2019.105439, 2020a.

Wang, L., Wu, C. Z., Gu, X., Liu, H. L., Mei, G. X., and Zhang, W. G.: Probabilistic stability analysis of earth dam slope under transient seepage using multivariate adapti ve regression splines, Bull. Eng. Geol. Environ., 79, 2763–2775, http://dx.doi.org/10.1 007/s10064-020-01730-0, 2020b.

Wang, R.: A simple orthonormalization method for stable and efficient computation of G reen's functions, B. Seismol. Soc. Am., 89, 733–741, 1999.

Wang, W., Yin, Y., Zhu, S., Wang, L., Zhang, N., and Zhao, R.: Investigation and num erical modeling of the overloading-induced catastrophic rockslide avalanche in Baige, Tibet, China, Bull. Eng. Geol. Environ., 79, 1765-1779, https://doi.org/10.1007/s10064 -019-01664-2, 2020c.

Wang, Y. F., Dong, J. J., Cheng, Q. G.: Velocity-dependent frictional weakening of large rock avalanche basal facies: Implications for rock avalanche hypermobility?, J. Geop hys. Res.-Sol. Ea., 122, 1648-1676, https://doi.org/10.1002/2016JB013624, 2017.

Wang, Y. F., Dong, J. J., Cheng, Q. G.: Normal stress-dependent frictional weakening of large rock avalanche basal facies: Implications for the rock avalanche volume effec t, J. Geophys. Res.-Sol. Ea., 123, 3270-3282, https://doi.org/10.1002/ 2018JB015602, 2 018.

Xu, Q., Zheng, G., Li, W. L., He, C. Y., Dong, X. J., Guo, C., and Feng, W. K.: Stud y on Successive Landslide Damming Events of Jinsha River in Baige Village on Oc tober 11 and November 3, 2018, J. Eng. Geo, 26, 1534-1551, https://doi.org/10.1354 4/j.cnki.jeg.2018-406, 2018. (In Chinese)

Yamada, M., Matsushi, Y., Chigira, M., Mori, J.: Seismic recordings of landslides caused by Typhoon Talas (2011), Japan, Geophys. Res. Lett., 39, L13301, http://doi.org/10. 1029/2012gl052174, 2012.

Yamada, M., Kumagai, H., Matsushi, Y., and Matsuzawa, T.: Dynamic landslide processe s revealed by broadband seismic records, Geophys. Res. Lett., 40, 2998–3002, https:/ /doi.org/10.1002/grl.50437, 2013.

Yamada, M., Mangeney, A., Matsushi, Y., and Moretti, L.: Estimation of dynamic frictio n of the Akatani landslide from seismic waveform inversion and numerical simulatio n, Geophys. J. Int., 206, 1479–1486. https://doi.org/10.1093/gji/ggw216, 2016.

Yamada, M., Mangeney, A., Matsushi, Y., and Matsuzawa, T.: Estimation of dynamic fri ction and movement history of large landslides, Landslides, 15, 1963–1974, https://do i.org/10.1007/s10346-018-1002-4, 2018.

Yan, Y., Cui, P., Chen, S., Chen, X., Chen, H., and Chien, Y.: Characteristics and inter pretation of the seismic signal of a field-scale landslide dam failure experiment, J. Mt. Sci., 14(2): 219–236. https://doi.org/10.1007/s11629-016-4103-3, 2017.

Yan, Y., Cui, Y., Guo, J., Hu, S., Wang, Z., and Yin, S.: Landslide reconstruction using seismic signal characteristics and numerical simulations: Case study of the 2017 "6.

24" Xinmo landslide, Eng. Geol., 270, 105582, http://doi.org/10.1016/j.enggeo.2020.105582, 2020a.

Yan, Y., Cui, Y., Tian, X., Hu, S., Guo, J., Wang, Z., Yin, S., and Liao, L.: Seismic signal recognition and interpretation of the 2019 "7.23" Shuicheng landslide by seismogram stations, Landslides, 17, 1191-1206, http://doi.org/10.1007/s10346-020-01358-x, 2020b.

Yu, D., Huang, X., and Li, Z.: Variation patterns of landslide basal friction revealed from long-period seismic waveform inversion, Nat. Hazards, 100, 313–327, https://doi.org/10.1007/s11069-019-03813-y, 2020.

Zhang, L., Xiao, T., He, J., and Chen, C.: Erosion-based analysis of breaching of Baige landslide dams on the Jinsha River, China, in 2018, Landslides, 16, 1965-1979, https://doi.org/10.1007/s10346-019-01247-y, 2019.

Zhang, S. L., Yin, Y. P., Hu, X. W., Wang, W. P., Zhang, N., Zhu, S. N., and Wang, L. Q.: Dynamics and emplacement mechanisms of the successive Baige landslides on the Upper Reaches of the Jinsha River, China, Eng. Geol., 278, 105819, http://dx.doi.org/10.1016/j.enggeo.2020.105819, 2020a.

Zhang, Z., He, S., Liu, W., Liang, H., Yan, S., Deng, Y., Bai, X., and Chen, Z.: Source characteristics and dynamics of the October 2018 Baige landslide revealed by broadband seismograms, Landslides, 16, 777-785, http://doi.org/10.1007/s10346-019-01145-3, 2019.

Zhang, Z., He, S., and Li, Q.: Analyzing high-frequency seismic signals generated during a landslide using source discrepancies between two landslides, Eng. Geol., 272, 105640, https://doi.org/10.1016/j.enggeo.2020.105640, 2020b.

Zhao, J., Moretti, L., Mangeney, A., Stutzmann, E., Kanamori, H., Capdeville, Y., Calder, E. S., Hibert, C., Smith, P. J., Cole, P., and Lefriant, A.: Model space exploration for determining landslide source history from long-period seismic data, Pure Appl. Geophys., 172, 389–413, https://doi.org/10.1007/s00024-014-0852-5, 2015.

Zhao, J., Ouyang, C. J., Ni, S. D., Chu, R. S., and Mangeney, A.: Analysis of the 2017 June Maoxian landslide processes with force histories from seismological inversion and terrain features, Geophys. J. Int., 222, 1965–1976, https://doi.org/10.1093/gji/ggaa226, 2020.

Zhou, L., Fan, X., Xu, Q., Yang, F., and Gou, C.: Numerical simulation and hazard prediction on movement process characteristics of Baige landslide in Jinsha river, Eng. Geol., 27, 1395-1404, https://doi.org/10.13544/j.cnki. jeg. 2019-037, 2019. (In Chinese)